Chemical Engineering Journal 500 (2024) 157384

Contents lists available at ScienceDirect

Chemical Engineering Journal

journal homepage: www.elsevier.com/locate/cej

Film-immobilized carbon nitride for the degradation of pharmaceuticals: A continuous flow photoreactor performance upheld by excitation-emission matrix fluorescence spectroscopy

Manuel Peñas-Garzón [a,b,*], Maria J. Sampaio [a,b], Ana M. Chávez [a,b,c], Adrián M.T. Silva [a,b], Cláudia G. Silva [a,b], Joaquim L. Faria [a,b,*]

[a] LSRE-LCM – Laboratory of Separation and Reaction Engineering - Laboratory of Catalysis and Materials, Faculty of Engineering, University of Porto, Rua Dr. Roberto Frias, 4200-465 Porto, Portugal
[b] ALiCE – Associate Laboratory in Chemical Engineering, Faculty of Engineering, University of Porto, Rua Dr. Roberto Frias, 4200-465 Porto, Portugal
[c] Departamento de Ingeniería Química y Química Física, Instituto Universitario del Agua, Cambio Climático y Sostenibilidad (IACYS), Universidad de Extremadura, 06006 Badajoz, Spain

ARTICLE INFO

Keywords:
Graphitic carbon nitride (g-C_3N_4)
Supported photocatalyst
Wastewater treatment
Continuous flow operation
EEM-PARAFAC

ABSTRACT

The validation of immobilized photocatalysts is a fundamental matter regarding the scaling-up process in the photocatalytic degradation of aqueous pollutants in natural surface waters. This work presents the comprehensive evaluation of graphitic carbon nitride (g-C_3N_4, CN) immobilized onto a polymeric film (F) placed inside a continuous flow operation planar reactor for the removal of a mixture of pharmaceuticals (*i.e.*, venlafaxine, citalopram, carbamazepine, tramadol, ketoprofen, and diclofenac, 3 μM each) under visible light. The resulting CN/F (8 mg of CN per cm^2 of film and with significant preservation of optical and structural properties after more than 350 h of reuse) yielded the complete removal under total recirculation of all pharmaceuticals after 90 min under visible light, except for ketoprofen, probably ascribed to competition for photogenerated holes, as suggested by the proposed mechanism. Under dead-end continuous flow mode, the steady-state conversion averaged 67% in deionized water, increasing up to 76%, and 80% in natural surface waters obtained from the Douro River and the effluent from a wastewater treatment plant (Northwestern Portugal), respectively, related to the promotion effect of carbonates anions and organic matter. The assessment of excitation-emission matrix (EEM) fluorescence spectroscopy coupled with parallel factor (PARAFAC) analysis further demonstrated the removal (*ca.* 50%) of the protein- and humic-like substances contained in the collected wastewater, thus evidencing the continuous flow mode performance of the immobilized photocatalyst for real environmental applications.

1. Introduction

The potential implementation of heterogeneous photocatalysis, as one of the most representative advanced oxidation processes (AOPs), for environmental applications, is usually related to some challenges, including the need to support the semiconductor (known as photocatalyst) particles to reduce or even avoid post-reaction recovery stages [1,2]. The support should gather specific requisites, specifically when used to treat contaminated aqueous solutions, including good adhesion with the supported photocatalyst, chemical stability under the reaction conditions, and hydrophobic properties [3]. Recent studies have evaluated the activity of the most investigated photocatalyst, *i.e.,* titanium dioxide (TiO_2), anchored on different supports. For instance, nitrogen-doped TiO_2 immobilized on poly(methyl methacrylate) demonstrated promissory results in the inactivation of pathogens [4], whereas the abatement of the antibiotic sulfamethoxazole was assessed using TiO_2 immobilized on glass wool and silica particles [1], showing a more stable photocatalytic performance when reusing the TiO_2/silica material compared to the glass wool; or even supported on glass beads [5].

Most of the previous examples entailed some alternatives to face the elevated energy required to activate the TiO_2 (*i.e.*, semiconductor band gap, E_g, around 3.2 eV), including the use of ultraviolet (UV) irradiation sources (including simulated solar light), or even the semiconductor modification (*e.g.*, by doping) to allow the harvesting of visible light. In

* Corresponding authors at: LSRE-LCM – Laboratory of Separation and Reaction Engineering - Laboratory of Catalysis and Materials, Faculty of Engineering, University of Porto, Rua Dr. Roberto Frias, 4200-465 Porto, Portugal.
E-mail addresses: manuelpgarzon@fe.up.pt (M. Peñas-Garzón), jlfaria@fe.up.pt (J.L. Faria).

https://doi.org/10.1016/j.cej.2024.157384
Received 22 July 2024; Received in revised form 25 October 2024; Accepted 2 November 2024
Available online 3 November 2024

this respect, a well-known visible-light-driven photocatalyst is graphitic carbon nitride (g-C_3N_4, $E_g \approx 2.7$ eV), characterized by its metal-free nature, cost-effective and facile preparation, good photocatalytic activity and long-term stability [6]. Immobilized g-C_3N_4 has also been recently tested for water purification purposes, evaluating different novel supports such as hydrogel spheres (chitosan- or alginate-based materials [7,8]), polyurethane foam [9] or membranes [10,11], exhibiting appropriate photocatalytic removals of common aqueous pollutants, such as antibiotics or industrial additives. Regarding the use of g-C_3N_4-based membranes, it should be noted that, despite the likely promissory combination of photocatalysis and filtration, the fact of the semiconductor being embedded in the membrane matrix may render the photocatalytic process less efficient.

Our research group has experience examining different carriers (*e.g.*, glass rings and cotton fabrics, to name a few) to immobilize g-C_3N_4 [12–14]. Besides, it was recently attempted the preparation of cylindrical supports obtained by additive manufacturing, confirming urea as a suitable g-C_3N_4 precursor [15]. In contrast, the one-pot *in-situ* procedure was validated as a promising methodology for coating the photocatalyst onto a ceramic alumina-based foam [16]. Considering photon absorption as a keystone in photocatalysis, the immobilization of the photocatalyst should involve effective utilization of the irradiated light, avoiding shaded spaces/areas [9]. Concerning this, the immobilization of g-C_3N_4 on polymeric film was successfully assessed to convert micropollutants contained in surface waters [17]. The poly(vinylidene fluoride)-based film used in that study gathers some of the aforementioned requirements for photocatalyst supports, including inertness, hydrophobicity, and high light resistance [18,19], to which we can add the necessary flexibility to facilitate installation across different reactor configurations. The good properties of films as photocatalyst supports, together with the scarce information still available, encourage us to continue investigating their potential application.

Moreover, there is increasing attention regarding the use of excitation-emission matrix (EEM) fluorescence spectroscopy coupled with parallel factor analysis (PARAFAC) for assessing not only the effect of photocatalysis on the degradation of contaminants but also the fluorescent soluble substances usually present in natural water samples (mainly proteins-like and humic-like substances) [20–22]. EEM-PARAFAC compiles the advantages of accessible data collection, high sensitivity, and quantitative description [23]. Even though Truong *et al.* recently reported the application of this methodology using g-C_3N_4 anchored on floating perlite in synthetic aqueous solutions [24], the precedent works were conducted using powder photocatalysts. Thus, the assessment of EEM-PARAFAC in natural water matrices using immobilized semiconductors lacks comprehensive studies to further realize their potential use.

In this context, this work aims to evaluate the photocatalytic performance of film-immobilized g-C_3N_4 for the removal of a mixture of pharmaceuticals (including antidepressants and analgesics) as target emerging contaminants due to their common detection in natural surface waters, high-resistance against conventional wastewater treatments and potential environmental effects [25,26]. The performance of the supported photocatalyst is evaluated in a continuous flow regime under visible irradiation (LED lights), firstly in recirculation mode concerning the optimization of the reaction parameters and afterward in dead-end configuration mode, addressing the treatment of real aqueous samples. The evolution of inherent fluorescent substances in the wastewater effluent was addressed through EEM-PARAFAC analysis, demonstrating the suitable performance of the immobilized carbon nitride for real water treatment applications.

2. Materials and methods

2.1. Reagents and materials

Urea (CH_4N_2O, 99.5%) was provided by Acros Organics. Poly (vinylidene fluoride) (PVDF, > 99%), poly(vinylpyrrolidone) (PVP, > 99%), 1-methyl-2-pyrrolidone (NMP, 99.5%), venlafaxine (VFX) hydrochloride (> 99%), tramadol (TMD) hydrochloride (≥ 99%), diclofenac (DCF) sodium salt (≥ 99%), and ketoprofen (KET, ≥ 98%) were purchased from Sigma-Aldrich. Citalopram (CTP) hydrobromide (> 99%) was provided by Supelco. Carbamazepine (CBZ, 98%) and 2,2,6,6-tetramethyl-1-piperidinyloxy (TEMPO, ≥ 98%) were obtained from Alfa Aesar. Triethanolamine (TEOA, 99%) was purchased from PanReac AppliChem. Sodium sulfate (Na_2SO_4; > 99%), sodium chloride (NaCl; ≥ 99%), and sodium hydrogen carbonate ($NaHCO_3$; ≥ 99%) were provided by Riedel-de-Haën, Fluka, and Honeywell, respectively. Acetonitrile (ACN, LC-MS grade), and 2-propanol (≥ 98%) were purchased from VWR Chemicals, and formic acid (> 99.5%) was provided by Merck.

Unless otherwise indicated, all preparations and experiments were performed using deionized water (DW). Two natural surface water samples were also used, collected from the Douro River (river water sample, herein labeled as RW sample), and from a secondary-treatment effluent from an urban wastewater treatment plant (WW sample), both located in Northwestern Portugal.

2.2. Immobilization of carbon nitride on film and characterization

Firstly, g-C_3N_4 (labeled as CN in this study) was obtained following a one-step synthesis previously described [15,16,27]. Briefly, urea (40 g) was placed in a closed crucible and submitted to thermal polymerization (ramp of 2 °C·min^{-1}) at 450 °C for 2 h and 550 °C for 4 h using a muffle furnace SNOL 8.2/1100. After cooling down, the resulting solid was washed with DW, dried overnight at 100 °C, and finally sieved (below 500 μm) before being stored until use. On the other hand, the polymeric solution used for preparing the film (labeled as F) was obtained following the steps reported elsewhere [15,17,19]. Concisely, PVP (0.07 g) was dissolved at room temperature in NMP (6 mL) under sonication for 3 h. Subsequently, PVDF (1.07 g) was incorporated into the previous solution and heated at 40 °C for 48 h under continuous stirring. The resulting polymeric solution was stored in a glass vial until use.

The CN immobilized on F (CN/F) was obtained following three simple stages (Fig. 1): a) the polymeric solution was uniformly distributed (covering a surface of 15.5 × 9.4 cm^2) over a glass plate (previously cleaned with ethanol and DW) using an Elcometer 3580 casting knife film applicator [11,17]; b) the CN powder was dispersed over the surface of the polymeric solution; and c) the powder immobilization was promoted by phase inversion adding DW over the glass plate, allowing the easy separation of the resulting film, containing the immobilized CN, from the plate. The resulting CN/F (consisting of around 8 mg of CN per cm^2 of film) was finally stored in DW.

The morphology of the samples was analyzed using an FEI Quanta 400 FEG ESEM microscope with secondary electrons (SE) mode. The N_2 adsorption–desorption isotherms (–196 °C) were obtained using a Quantachrome Nova 4200e apparatus. The specific surface was estimated by means of the Brunauer-Emmett-Teller method. The optical properties were analyzed by ultraviolet–visible diffuse reflectance spectroscopy (UV–Vis DRS), using a JASCO V-560 spectrophotometer equipped with a JASCO ISV-469 integrating sphere attachment using $BaSO_4$ as reference material. The Tauc plot method [28] was followed to estimate the band gap values (E_g), considering CN as an indirect semiconductor [29]. The photoluminescence (PL) properties of solids materials were examined using a JASCO FP-8300 spectrofluorometer, setting the excitation wavelength at 370 nm and bandwidth (excitation and emission) of 2.5 nm. Emission spectra were recorded directly without applying any spectral correction. The Fourier transform infrared (FTIR) transmittance was determined by attenuated total reflectance (ATR) using a JASCO FT/IR-6800 equipped with a MIRacle^{TM} single reflection attenuated total reflectance ZnSe crystal plate accessory (PIKE Technologies), analyzing the wavenumber range of 4000–600 cm^{-1} with a resolution of 4 cm^{-1}.

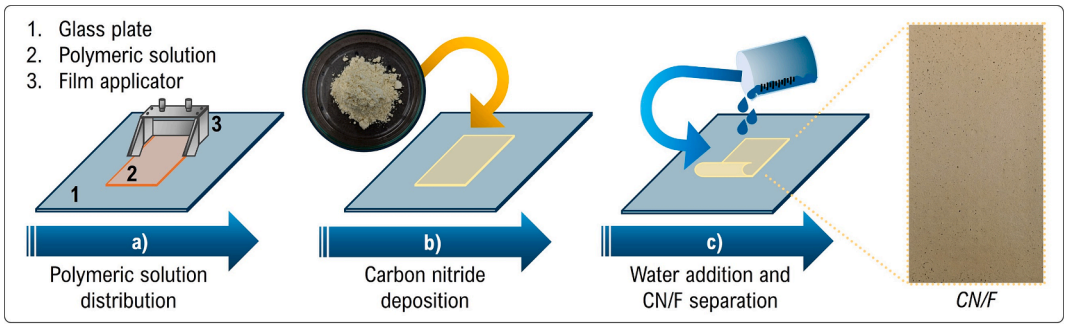

Fig. 1. Scheme of the sequential steps followed in the preparation of the carbon nitride immobilized on the polymeric film.

2.3. Photocatalytic setup

Fig. 2 schematizes the experimental setup and collects the main information about the light sources used in this study. The CN/F was placed between the two acrylic plates of the photoreactor (NETmix system), with a reaction volume of 30 mL. In this respect, the patented static mixer NETmix is composed of a regular network of interconnected rectangular channels (2 mm height × 1 mm width) and circular chambers (2 mm height × 7 mm diameter) [30], originally developed as a mixing reactor for the preparation of hydroxyapatite nanoparticles [31], and subsequently evaluated as planar photoreactor (mainly for Fenton-mediated photocatalysis [32–34]), taking advantage of the larger irradiated surface area per unit of liquid volume inside the reactor.

The photoreactor was placed vertically inside the LEDs box (Fig. 2**a**), equipped with two aligned visible LEDs (average λ_{max} = 415 nm and full width at half maximum (FWHM) = 15 nm, Fig. 2**b**) at 3.5 cm from the upper and lower limits of the NETmix system. Average irradiances between 520 and 140 W·m^{-2} at distances between 4 and 10 cm, respectively, from the CN/F to the light sources (as depicted in Fig. 2**c**) were measured using an OceanOptics USB2000 + spectroradiometer.

All the experiments in this study were carried out in a continuous flow regime using a peristaltic pump. Firstly, the reaction parameters (*i.e.*, distance from LEDs to the immobilized photocatalyst, the recirculation flow rate, or the treated aqueous volume) following a total recirculation mode (indicated by the dash lines in Fig. 2**a**) were investigated, whereas a dead-end mode was assessed to investigate the photocatalytic performance in the treatment of different water matrices. Unless otherwise indicated, the total recirculation mode was assessed using 100 mL DW spiked with VFX (3 μM, approx. 830 μg·L^{-1}). In this sense, VFX was selected as the target pharmaceutical for these preliminary studies concerning its representative chemical structure, as well as its common detection in current surface waters [35,36], resulting in the inclusion of this compound in the Watch List of substances for European Union monitoring in surface water [37], and in the list of micropollutants to be monitored in urban wastewater treatment according to the new proposal for a European directive in this domain. The photocatalytic performance was also evaluated using a mixture of six pharmaceuticals (including the antidepressants VFX, CTP, and CBZ; and the analgesics TMD, KET, and DCF; 3 μM each). All experiments were carried out without varying the initial pH (natural pH within the range of 6.8–7.1). The total recirculation mode experiments were carried out considering the equivalent irradiation time (t_{eq}), as indicated in **Eq. (1)**

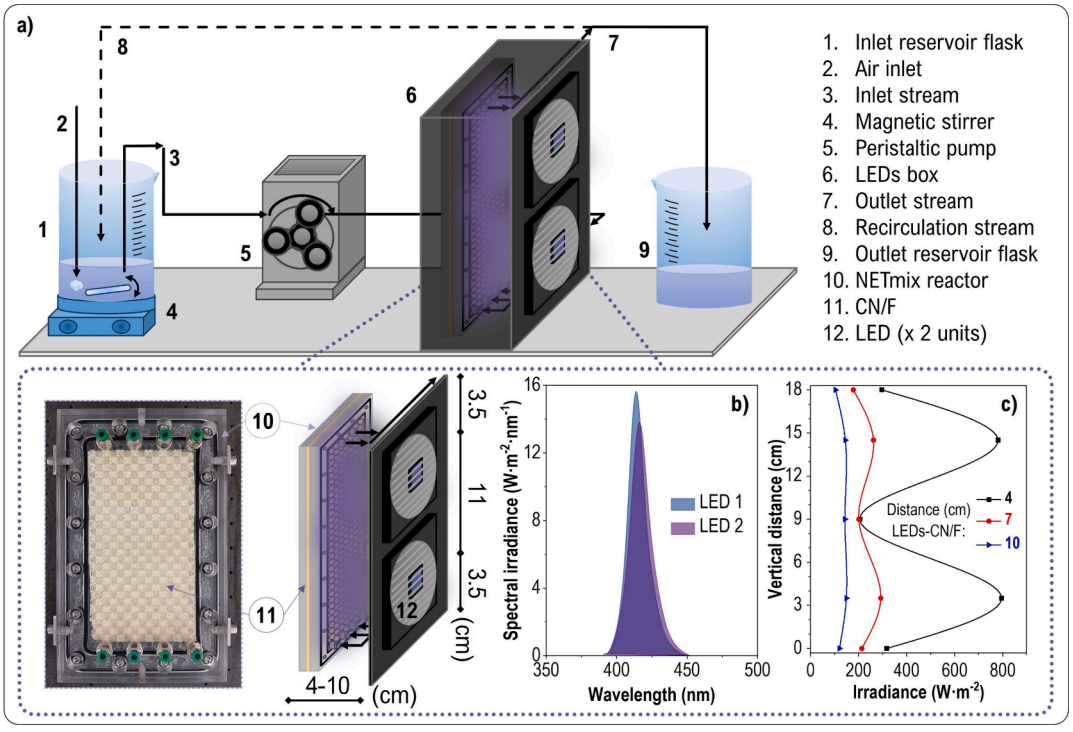

Fig. 2. a) Scheme of the photocatalytic setup; b) irradiance distribution considering the distance between the CN/F and the LEDs; and c) spectral irradiance of the LEDs.

[32,38]:

$$t_{eq} = t_r \cdot \frac{V_R}{V_T}, \quad (1)$$

being t_r the reaction time in the recirculation system (min), V_R and V_T the volume inside the reactor and the total solution volume (L), respectively. The effect of different scavengers was assessed using 2-propanol, TEOA, and TEMPO to quench $HO^{\bullet}$, h^+, and $O_2^{\bullet-}$, respectively [39–41] (the constant rates being $k_{[2\text{-}propanol,\ HO^{\bullet}]} = 1.9 \cdot 10^9$ $L \cdot mol^{-1} \cdot s^{-1}$ [42], and $k_{[TEMPO,\ O2^{\bullet-}]} = 1.2 \cdot 10^5$ $L \cdot mol^{-1} \cdot s^{-1}$ [43]). Besides analyzing the effect on the conversion of each contaminant, the conversion of equivalent total carbon from initial compounds (X_{Ceq}) was considered following **Eq. (2)**:

$$X_{C_{eq}}(\%) = \left(1 - \frac{\sum C_{iC,t}}{\sum C_{iC,0}}\right) \cdot 100 \quad (2)$$

being $\Sigma C_{iC,t}$ and $\Sigma C_{iC,0}$ the sum of the equivalent atomic carbon concentration from the initial compounds at reaction t and 0, respectively.

The effect of the water matrix was investigated in continuous dead-end mode. Unless otherwise indicated, the natural water samples were spiked with the mixture of the six pharmaceuticals (3 μM each) at natural pH, and the photocatalytic removal was evaluated using a hydraulic retention time (τ) of 100 min. The effect of specific anions was investigated by adding NaCl, Na_2SO_4, and $NaHCO_3$ to DW.

For both continuous flow regime modes, the solution containing the spiked contaminants was passed through the reactor for 7–10 min (up to obtain a concentration similar to the initial one) to achieve the adsorption–desorption equilibrium prior to the beginning of the irradiation ($t = 0$ min). The solution in the inlet reservoir was kept under constant stirring and saturated with air (~50 $mL \cdot min^{-1}$, using an air pump). Two fans coupled to the LEDs allowed to keep the temperature around 26 ± 2 °C throughout the experiments. After each experiment, the CN/F and the reactor were washed with DW. All experiments were performed twice. The average value was included and, in case of a difference of more than 4% in the duplicates, a third experiment was performed.

2.4. Analytical techniques and EEM-PARAFAC methodology

A Nexera X2 LC-30AD apparatus was used to determine the concentration of the pharmaceuticals by ultra high-pressure liquid chromatography (UHPLC). The system is equipped with an RF-20A XS fluorescence detector (allowing the determination of TMD, VFX, and CTP using $\lambda_{exc} = 230$ nm and $\lambda_{emi} = 300$ nm) and an SPD-M20A diode array detector (being identified KET, DCF, and CBZ at $\lambda_{exc} = 256$, 276 and 285 nm, respectively). A reverse phase column Kinetex™ XB-C18 (100 Å, 100 × 2.1 mm i.d., 1.7 μm particle diameter) was used, with a mobile phase comprised of a mixture of 0.1% formic acid in ultrapure aqueous solution/ACN (A/B). The gradient method started with a proportion of ACN of 18%, and gradually increased up to 60% after 12 min, using a flow of 0.25 $mL \cdot min^{-1}$ at 30 °C. Once determined the concentration at irradiation times 0 and t (min), C_0 and C_t, respectively, the photocatalytic conversion (X, %) was calculated following the expression $X = (1\text{-}C_t/C_0) \cdot 100$. The conversion data were then non-linear fitted by using the apparent pseudo-first-order kinetic model ($X = (1\text{-}e^{-kapp \cdot t}) \cdot 100$), being k_{app} (min^{-1}) the apparent pseudo-first-order rate constant.

The natural water samples were characterized (Table 1) following standard methods [44]. A pH/ion 7372 WTW pHmeter and a HI88703 turbidimeter were used for the determination of the pH and turbidity values, respectively. The chemical oxygen demand (COD) was determined by colorimetry. A Shimadzu TOC-5000A analyzer was used to determine the total organic carbon (TOC). The detection of anions (using corresponding standard solutions) was performed by ionic chromatography (IC) using a Metrohm 881 Compact IC pro apparatus, under isocratic conditions using a mobile phase (0.7 $mL \cdot min^{-1}$) of 3.6 mM $NaHCO_3$ and Metrosep A Supp 7 column (250 × 4 mm, 5 μm particle diameter) as stationary phase, also provided with chemical and CO_2 suppressor modules (MSM and MCS, respectively).

Table 1
Physicochemical characterization of the water matrices used in this study.

Parameters	Deionized water (DW)	River water (RW)	WWTP effluent (WW)
pH	6.86	7.55	7.45
Turbidity (NTU)	0.20	0.75	4.60
Conductivity ($\mu S \cdot cm^{-1}$)	5.5	241.0	808.0
TSS ($mg \cdot L^{-1}$)	< 0.1	1	14
COD (mg $O_2 \cdot L^{-1}$)	< LOD (3.53)	< LOD (3.53)	37.10
TOC (mg $C \cdot L^{-1}$)	0.53	4.10	12.81
HCO_3^- ($mg \cdot L^{-1}$)	3.28	53.03	229.67
SO_4^{2-} ($mg \cdot L^{-1}$)	0.18	18.13	37.19
PO_4^{3-} ($mg \cdot L^{-1}$)	< LOD (0.006)	< LOD (0.006)	< LOD (0.006)
NO_2^- ($mg \cdot L^{-1}$)	< LOD (0.003)	0.14	0.18
NO_3^- ($mg \cdot L^{-1}$)	0.24	2.13	0.15
Cl^- ($mg \cdot L^{-1}$)	2.08	17.97	86.68

TSS: Total suspended solids; COD: Chemical oxygen demand; TOC: Total organic carbon; NTU: Nephelometric turbidity units; LOD: Limit of detection.

Excitation-emission matrix (EEM) fluorescence spectroscopy was registered using a JASCO FP-8300 apparatus. The excitation wavelength range was set in the range 210–500 nm (intervals of 2 nm), whereas the emission range was analyzed in the range 220–500 nm (0.5 nm step). Fluorescence data were recorded at 5000 $nm \cdot min^{-1}$, being the bandwidths of excitation and emission of 5 nm. A negligible inner-filter effect was observed in water samples. MATLAB R2018a was used to perform the PARAllel FACtor (PARAFAC) modeling. Firstly, the fluorescence data were processed for light scattering correction using the 'EEM_corr' chemometric software [45], allowing the mitigation of Raman and Rayleigh scattering [46]. Secondly, the corrected EEM spectra were decomposed using the second-order multivariate calibration toolbox 'mvc2_gui' [47]. A trilinear decomposition (TLD) was performed fixing non-negativity constraints for A (scores), B (excitation), and C (emission) modes. EEM spectra were decomposed using the PARAFAC modeling on three different zones, predicting up to 5 components for each zone, and finally, those that gathered the most plausible validation according to the following procedure [48] were selected: i) core consistency test (CCT) > 50; ii) low and constant standard deviation residues (SDR); and iii) excitation/emission profiles related to the EEM spectra.

3. Results and Discussion

3.1. CN and CN/F characterization

Fig. 3 collects the SEM images of the CN powder and immobilized on the film. The CN powder (Fig. 3**a**) is characterized by a high disorder of thin nanosheets. Indeed, it has been previously described the effect of using urea as CN precursor [15,49], yielding materials with a higher degree of exfoliated sheets compared to other precursors (*e.g.*, dicyandiamide or melamine), probably as a consequence of the higher release of gas bubbles (mainly CO_2 and NH_3) during the thermal polymerization [50]. In contrast to the smooth surface observed in the bare film (**Figure S1**), the immobilized sample (Fig. 3**b**) depicts a rough appearance due to the distribution of the photocatalyst over the surface. The magnification depicted in Fig. 3**c** confirms the absence of apparent variations in the powder morphology after immobilization. Fig. 3**d** shows the cross-section of CN/F, where the two main phases comprising the CN/F can be observed, *i.e.*, a polymeric film (with an average thickness of around 180 μm) supporting the immobilized powder photocatalyst. Besides, the CN/F was also analyzed after all the experiments included in this study (above 350 h of photocatalytic treatment), being observed minimal variations in the morphology (Fig. 3**e,f**), which can be attributed to expected attrition after consecutive runs.

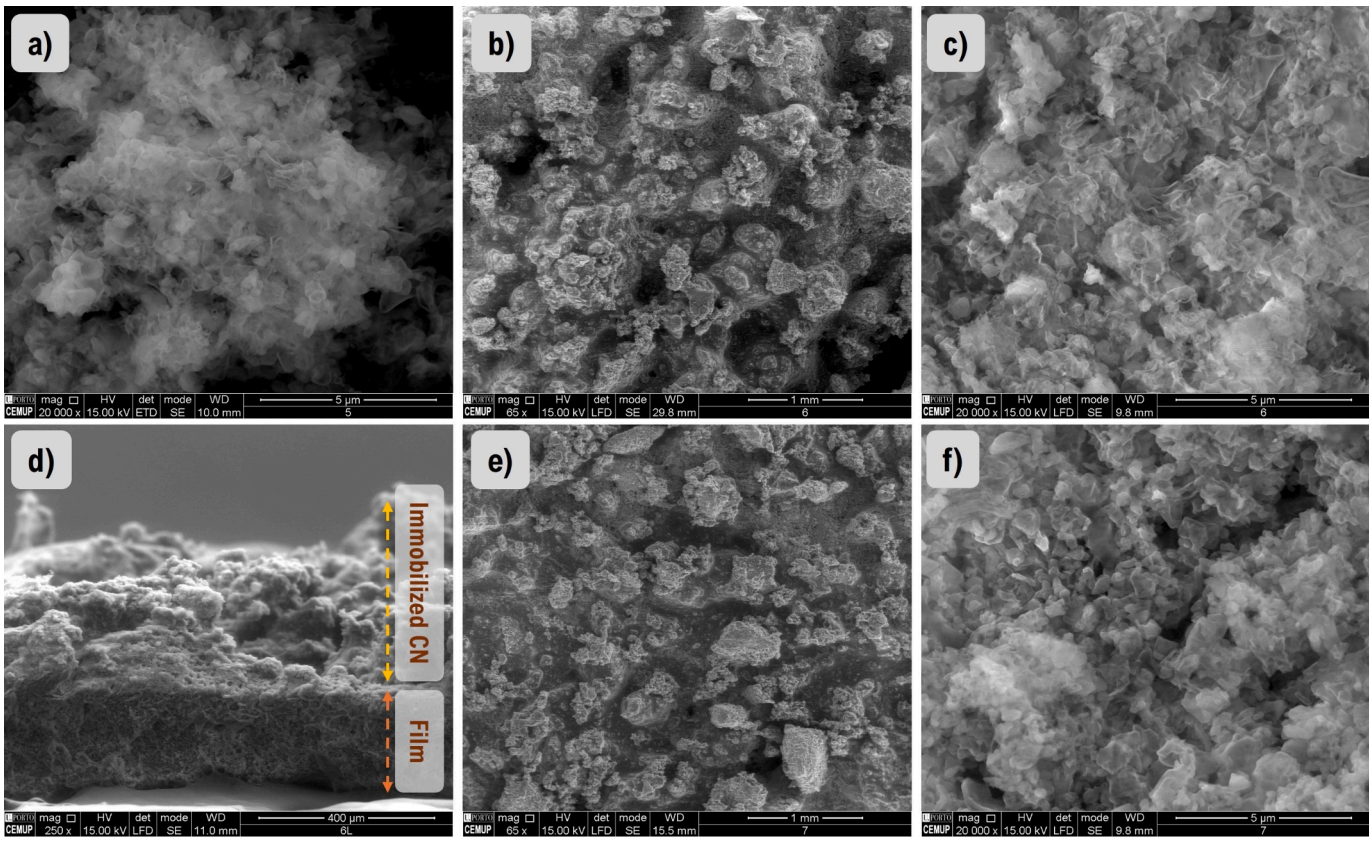

Fig. 3. SEM micrographs of CN powder (a), and CN/F before (b, c; and cross-section image d), and after repeated photocatalytic treatment (e, f) at different magnifications.

The texture of the synthesized samples was also analyzed (**Figure S2**), confirming the main mesoporous character of the powder sample (specific area of approximately 40 $m^2 \cdot g^{-1}$) as observed by the type II isotherm including an H3 hysteresis loop [15,51]. On the other hand, the immobilized CN/F was characterized by a low surface area (around 5 $m^2 \cdot g^{-1}$, which is within the range of measurement uncertainty), as a consequence of the negligible porous development of the polymeric film (results not shown). Besides, the specific area of the supported sample was mainly maintained after long-term use.

The optical and structural properties of powder and immobilized CN materials were also examined (Fig. 4). However, due to the previous extensive characterization of CN prepared from urea reported by our research group and collaborators [15,16,49], the results here included aims at confirming the adequate preparation of the materials. Briefly, the light absorption profiles (Fig. 4**a**) display an intensity absorption above 50% up to 405–410 nm, without a significant light absorption depicted by the pristine film (F sample). The higher intensity observed for the immobilized samples was then ascribed to slight differences in the analysis setup (in contrast to the solid sample holder, a film holder without a quartz window was used for immobilized samples). However, the effect is negligible regarding the absorption edge (inset of Fig. 4**a**), and the constant band gap energy of 2.78 eV (estimated from the respective Tauc plots, Fig. 4**b**). The PL emission spectra depicted in Fig. 4**c** agree with the CN-related materials previously indicated. Furthermore, the similar normalized spectra collected at the inset of Fig. 4**c** confirm that the lower PL intensity of immobilized CN may be due to some interference with the film rather than a quenching effect ascribed to the recombination of photogenerated charges [17].

Regarding the chemical structure of the samples (Fig. 4**d**), the immobilized CN presents the characteristic functional surface groups ascribed to the powder photocatalyst (as proved by the presence of stretching (υ) and bending (δ) vibrations of C = N (ii), and C-N (iii), as well as the vibrations modes of the s-triazine rings (iv) [52]). In this respect, the results concerning the powder CN agrees with the chemical composition previously reported (following XPS characterization) [49] of powder carbon nitride prepared by a similar heat polymerization process, in which the significant contribution of C-$(N)_2$, N-$(C)_2$, N–H, or N-$(C)_3$ bonds was proved. In our work, the CN immobilization on the film is evidenced by the presence of C-F_2 symmetric stretching and = C–H vibration modes (around 1177 and 1071 cm^{-1}, respectively) [53,54], similar to those found in the film counterpart, characteristics of the β-phase of PDVF-based polymers. In addition, an intense band around 1399 cm^{-1} (within the aforementioned region iii) is observed in CN/F and F samples, which could be related to the presence of C-N vibrations from the NMP and PVP precursors used in the film preparation. A general lower transmittance intensity was registered for immobilized samples, ascribed to the interference with the film, except in the range of the stretching vibrations of N–H, N-H_2, and adsorbed water molecules (i), probably as a consequence of storing the CN/F in deionized water. Overall, the used CN/F presents lower intensity, which can be attributed to the previously indicated attrition of the material after consecutive runs, in agreement with the characterization described above.

3.2. *Photocatalytic performance of the film-immobilized carbon nitride*

3.2.1. *Continuous total recirculation mode*

Optimization of operating conditions

Preliminary tests (**Figure S3**) validated placing the CN/F photocatalyst at a distance from LEDs between 4–7 cm (517–238 $W \cdot m^{-2}$, respectively), due to a reduction of photocatalytic performance in the removal of VFX when placing at 10 cm (140 $W \cdot m^{-2}$). This apparent indifference of reaction rate at high irradiation values was previously described [55,56]. According to these studies, the photocatalytic performance is proportional to the intensity for low irradiance values (*i.e.,*

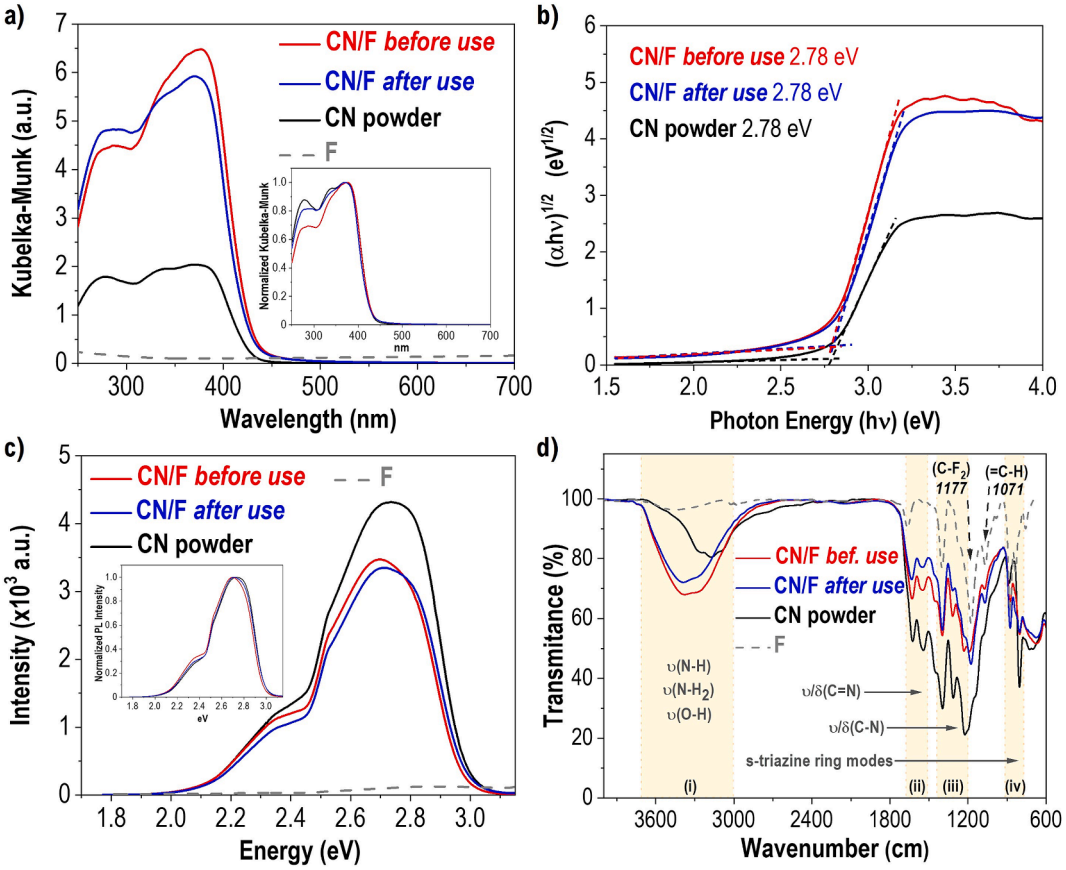

Fig. 4. A) UV–Vis DRS, b) Tauc plot, c) PL spectra, and d) FTIR-ATR of the CN powder and CN/F before and after repeated use. The normalized intensities have been included in UV–Vis DRS and PL spectra for comparison.

< 200 W·m^{-2}), being practically independent as the irradiance intensities increase as a consequence of the equilibration between the e^-/h^+ separation and recombination processes. Thus, the following experiments were carried out at a distance of ~ 5.5 cm from LEDs, being the average irradiance around 375 W·m^{-2}.

Fig. 5**a** depicts the evolution of the photocatalytic VFX conversion using a flow rate (Q) in the range of 0.5–20 mL·min^{-1} in recirculation mode. It can be observed that, as expected, the higher the flow rate, the higher the elimination of the target compound (even yielding more than 90% of VFX removed in less than 20 min of equivalent irradiation), as a consequence of the irradiation of a higher volume of the aqueous solution. However, and considering the time needed to yield a 70% conversion of the initial VFX (Fig. S4**a**), it can be observed the generation of a plateau as the flow rate increases, suggesting that the recirculation setup is following a certain approximation to a batch reactor configuration at flow rates around 20 mL·min^{-1}. Higher values would result in an increasing number of recirculation cycles together with a decreasing residence time, reaching a certain conversion equilibrium ascribed to the similar irradiation dose received [57]. In addition, and to characterize the flow regime inside the photoreactor, the Reynolds number (Re) was estimated (values among 0.4 and 15.8, **Table S1**), suggesting a laminar flow [33,55,58] following the current reactor

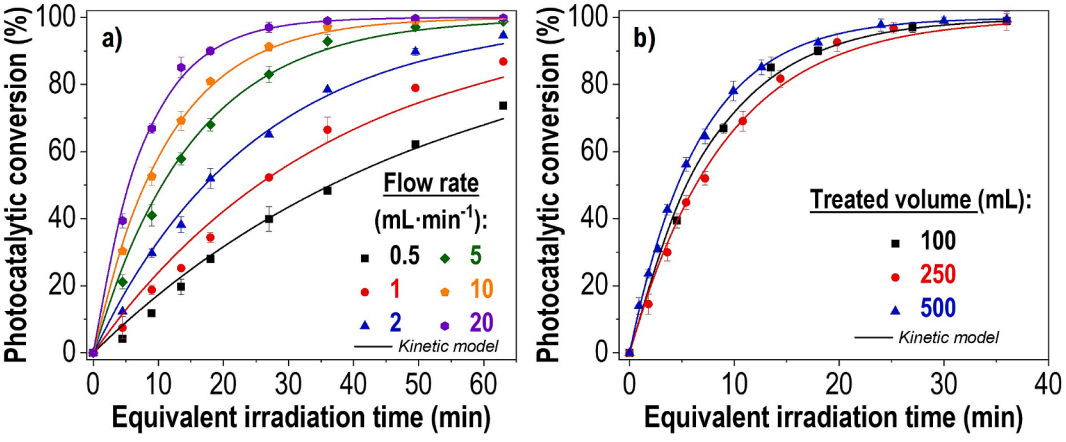

Fig. 5. A) Evolution of VFX photocatalytic conversion varying the flow rate, and b) the total solution volume under continuous total recirculation mode using CN/F. Apparent pseudo-first-order kinetic model fitting was included. $[VFX]_0 = 3$ μM; $[Irrad.]_{avg} = 375$ W·m^{-2}; Q (in figure b) = 20 mL·min^{-1}.

geometry. Therefore, the above-described removal trend can be complemented by improved mass transfer with increasing flow rate as a result of the increasing laminar mixing in the photoreactor chambers. In this sense, photocatalytic reactors following laminar flow hydrodynamics (usual values of Re < 50) are commonly found in previous studies [57,59], maximizing the residence time under the same irradiation conditions.

Fig. 5**b** displays the effect of varying the total volume treated. Despite the larger volumes requiring higher time to reach similar removal of the target pharmaceutical (Fig. S4**b**), the total recirculation mode allowed a similar photocatalytic performance regardless of the volume used considering the equivalent irradiation time (estimated using aforementioned **Equation (1)** needed to treat a certain solution volume.

Removal of pharmaceuticals in a mixture and oxidation mechanism

Once the main operating conditions concerning the continuous total recirculation mode were assessed, the performance of the film-immobilized CN in the photocatalytic elimination of a mixture of three antidepressants (VFX, CTP, and CBZ) and three analgesics (TMD, KET, and DCF) was evaluated. Fig. 6 shows that five pharmaceuticals from the mixture were totally converted under visible light after 90 min of treatment, with a remarkable removal above 80% in the first 36 min for VFX, CTP, DCF, and TMD. It also highlights the evolution of KET, which only yielded a removal of around 30% of the initial concentration, suggesting a strong competition for the species involved in the oxidation process.

Overall, these results confirm the potential of the immobilized CN for the photocatalytic abatement of different compounds. Despite the direct comparison should be carefully conducted due to the wide assortment of reaction conditions, **Table S2** summarizes some of the main results from previously reported immobilized semiconductors in the abatement of the pharmaceuticals investigated in this study, including the photocatalytic removal and the apparent pseudo-first-order rate constant (k_{app}) values. It can be observed that the film-immobilized CN herein studied presents photocatalytic activities comparable or even remarkably higher to those other relevant previous investigations. For instance, the k_{app} value ($10.25{\cdot}10^{-2}$ min^{-1}) of CN/F in the removal of VFX (in combination with other pharmaceuticals) is almost twofold that one previously reported by our group regarding the immobilization of g-C_3N_4 in 3D-printed poly(lactic acid) structures [15]; or one order of magnitude higher compared to the Ag-doped TiO_2 anchored on glass slides reported by Mokhtari *et al.* [60]. In these both examples, the setup consisted of cylindrical reactors under visible light, the photocatalyst being immersed in water layers above 10 mm, suggesting a determinant effect on the performance related to the diminution of light absorption due to the depth of the water layer (around 2 mm in the system evaluated in this study).

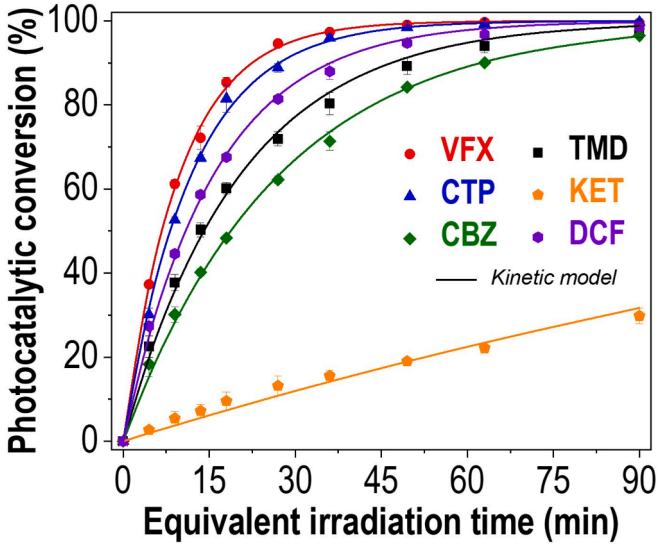

Fig. 6. Conversion of pharmaceuticals in a mixture under continuous total recirculation mode using CN/F in deionized water (DW). Apparent pseudo-first-order kinetic model fitting was included. $[Pharm.]_0 = 3$ μM each; $[Irrad.]_{avg} = 375$ $W{\cdot}m^{-2}$; $Q = 20$ $mL{\cdot}min^{-1}$.

A superior order of magnitude in the kinetic rates was also found in the conversion of CBZ compared to the reported use of g-C_3N_4 immobilized on chitosan-based hydrogel beads [7], and ZnO foams [57]. It should be noted that the irradiance in our study (375 $W{\cdot}m^{-2}$) was higher than that reported in these counterparts (*ca.* 156 and 104 $W{\cdot}m^{-2}$, respectively), despite the highly energetic light sources (simulated solar and UV lights, respectively) used throughout these examples. On the other hand, the conversion rate of DCF using the CN/F was similar to the TiO_2/glass beads system reported by Matoh *et al.* [5] ($6.38{\cdot}10^{-2}$ and $5.7{\cdot}10^{-2}$ min^{-1}, respectively). Concerning the uncertain possibility of releasing metallic elements into the treated waters, the metal-free composition of the immobilized photocatalyst proposed here represents a significant advantage regarding the potential application. **Table S2** also collects the main results obtained using different water matrices (RW, and WW; shown in **Figure S5**), under the total recirculation mode. However, due to specific similarities found with the results from the continuous dead-end configuration also investigated in this study, these results will be described in *section 3.2.2.* in further detail.

To examine the species involved in the oxidation process (mainly the hydroxyl and superoxide radicals, $HO^{\bullet}$ and $O_2^{\bullet-}$, respectively, and photogenerated holes, h^+), some quencher compounds were added to the solutions containing the contaminants. It should be noted that the use of scavengers is considered controversial because each of these compounds may have a certain affinity for the target species to be quenched, but parallel interactions (to a lesser extent) with other species involved in the process cannot be discarded. Accordingly, only a qualitative description of the results is provided in this work.

Concerning the global photocatalytic mechanism over the mixture of pharmaceuticals, the conversion of equivalent total carbon from initial compounds (X_{Ceq}, **Eq. (2)**) was considered. The results, shown in Fig. 7**a**, suggest a major contribution of $O_2^{\bullet-}$ and h^+ in the global photocatalytic mechanism, with a less pronounced, but still significant, role of $HO^{\bullet}$. In this sense, this minor role of $HO^{\bullet}$ was previously proved by Velo-Gala *et al.* [61] through kinetic modeling applied to the photocatalytic oxidation mechanism of phenol using graphitic carbon nitride. On the other hand, the specific contribution of the aforementioned species in the oxidation of each pharmaceutical is depicted in Fig. 7**b** (being the corresponding k_{app} values collected in **Table S3**), evidencing that each compound might follow a specific trend (also without neglecting the likely interactions among pharmaceuticals in the mixture). Following these results and the chemical structure of the compounds (**Table S4**), we can tentatively propose two main arrangements, namely *Group I*: compounds whose oxidation mechanism is mainly mediated by $O_2^{\bullet-}$/$HO^{\bullet}$ (including VFX, CTP, and TMD, all of them characterized by the presence of terminal tertiary amines and the co-presence of aromatic and non-aromatic rings in their structure), and *Group II*: compounds as CBZ, KET, and DCF (whose structure lacks terminal tertiary amines and all rings are aromatic), characterized by the main contribution of $O_2^{\bullet-}$/h^+ in their oxidation mechanism. Indeed, the higher affinity of h^+ towards amine fractions (present in the DCF and CBZ) due to its higher electron donor character (facilitating the oxidation through the formation of the radical-cation moieties, as previously described for g-C_3N_4-based materials by Samanta *et al.* [62]) could explain the aforementioned lower photocatalytic performance related to the conversion of KET.

Therefore, a tentative global photocatalytic mechanism was proposed. As schematized in Fig. 7**c**, the irradiation with the necessary energy ($E \geq E_g = 2.78$ eV, $\lambda \leq 446$ nm) may produce the separation of the e^-/h^+ pair, allowing the generation of $O_2^{\bullet-}$ and $HO^{\bullet}$ by interaction with dissolved oxygen and water molecules (−0.33 V and + 2.29 V *vs* NHE,

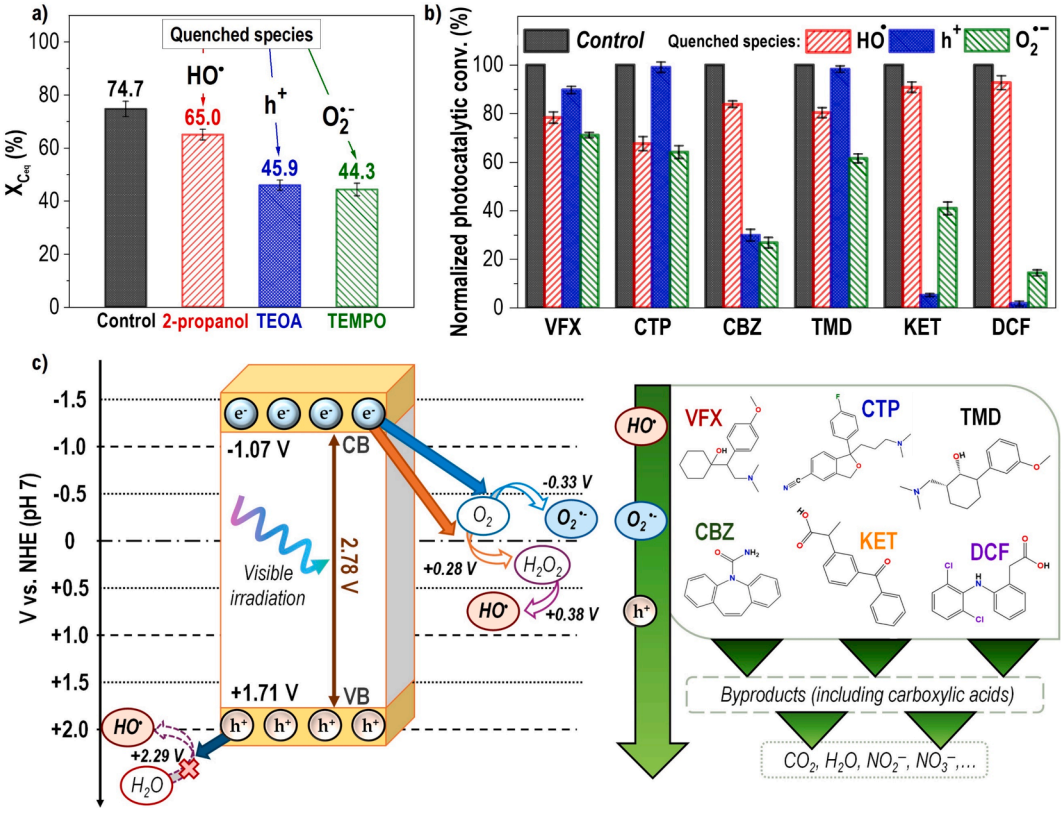

Fig. 7. A) Conversion of equivalent total carbon (X_{Ceq}), and b) normalized conversion of pharmaceuticals in mixture using CN/F and specific quenchers under continuous total recirculation mode (t_{eq} = 36 min). c) Scheme of the proposed photocatalytic mechanism. [Pharm.]$_0$ = 3 μM each; [Quencher]$_0$ = 1 mM; [Irrad.]$_{avg}$ = 375 W·m^{-2}; Q = 20 mL·min^{-1}.

pH 7 [63]) in the conduction (CB) and valence bands (VB), respectively. However, the electrochemical characterization of CN previously reported by our group [15], pointed out that the generation of HO$^\bullet$ from direct oxidation of water is prevented due to the more positive potential level of the CB (+1.71 V). Thus, and considering the proven contribution of HO$^\bullet$ in the conversion of the herein-investigated pharmaceuticals, the formation of the radical should be driven by another mechanism. In this sense, the intermediate generation of H_2O_2 as HO$^\bullet$ precursor using g-C_3N_4-based photocatalysts was previously demonstrated in several studies [61,64,65] through the 2e$^-$-mediated reduction of oxygen in slightly acidic media ($O_2 + 2H^+ + 2e^- \rightarrow H_2O_2$, +0.28 V *vs* NHE, pH 7 [66,67]) followed by the reduction of H_2O_2 to HO$^\bullet$ ($H_2O_2 + e^- \rightarrow HO^\bullet + HO^-$, +0.38 V *vs* NHE, pH 7 [67]). The generation of HO$^\bullet$ following this mechanism would leave the h^+ accessible at the VB to lead the overall conversion of the pharmaceuticals, in addition to $O_2^{\bullet-}$, as previously described. The oxidation of the contaminants may result in the formation of different byproducts, including short-chain carboxylic acids (such as oxalic, acetic, and formic acids, in anionic form detected by IC), and ultimate oxidation products as NO_2^-, NO_3^- (both identified by IC) and CO_2 (proved by TOC removal as described below).

3.2.2. *Continuous dead-end mode*

Water matrix influence

Once revealed the promising photocatalytic activity in the abatement of different compounds under continuous recirculation mode, the CN/F performance was evaluated in continuous dead-end mode considering its potential application in a more real context. Fig. 8**a-c** depicts the conversion of the pharmaceuticals spiked in different water matrices (including DW, and the surface water samples RW, and WW), yielding stationary conversions after 2–3 h of the irradiated stream under hydraulic retention time (τ) of 100 min. It can be observed that there is an upward trend in the removal yields of all pharmaceuticals when increasing the complexity (*i.e.*, organic and inorganic content, Table 1) of the aqueous solution, averaging steady-state conversions around 67%, 76%, and 80% for DW, RW, and WW, respectively. Fig. 8**a-c** also shows that the CN/F provides a steady-state conversion of the TOC around 30% after 6 h under visible irradiation, regardless of the aqueous solution tested.

In this respect, the influence of the water matrix on photocatalysis is controversial, with a wide variety of previous investigations pointing out a deactivating effect due to inorganic and organic compounds, generation of less reactive radicals, or light attenuation by increased turbidity [5,68–71]; whereas other studies describe the positive effect of pH, or dissolved organic matter, through the promotion of electron transfer and radical addition reactions, among other mechanisms [51,72–75]. It should be noted that most of these studies were carried out using suspended photocatalysts in slurry reactors, so a great influence of certain parameters (such as turbidity) when using more complex aqueous matrices can be expected. In this respect, our results suggest a negligible turbidity effect since the value of this parameter for DW increases between 3- and 20-folded for RW and WW, respectively. This can be ascribed to one of the main advantages of using the NETmix as a planar photoreactor, related to the low height of the chambers/channels network (2 mm), reducing the depth of the water layer above the immobilized photocatalyst, and maximizing the area exposed to light. To verify this, the irradiance was measured using different depths of the WW layer (**Figure S6**). The initial irradiance decreased by around 3% at a depth of 2 mm, reaching a 6% decrease at 10 mm. Concerning the pH, the contribution could be considered negligible due to the minor pH variation among the experiments (final pH values in the range of 7–8).

Photolysis results (usually below 10%), obtained in the absence of the immobilized photocatalyst (**Figure S7**), also suggest a certain higher removal of the contaminants spiked in RW and WW. Therefore, this increased conversion observed in natural water samples could be related

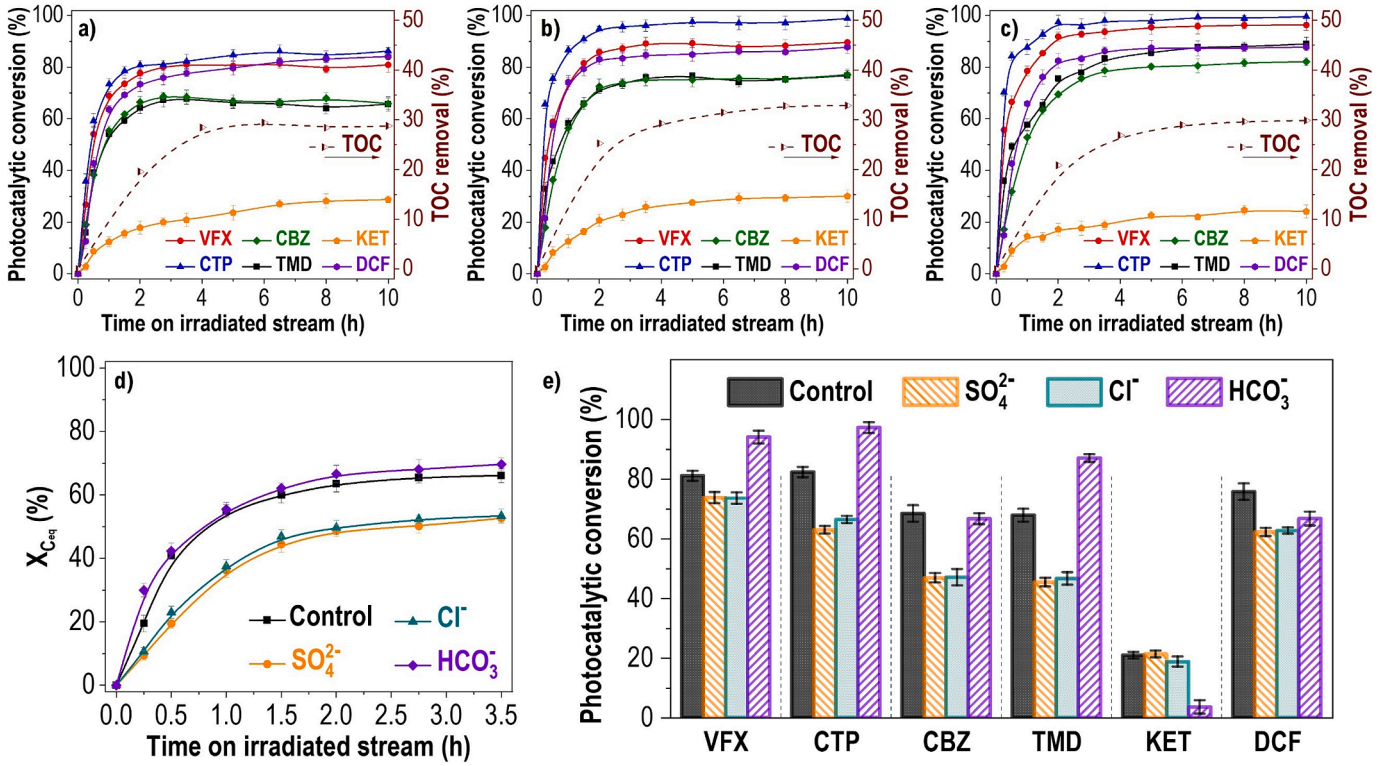

Fig. 8. Photocatalytic removal of the pharmaceuticals in a mixture spiked in deionized water (DW) (a), river water (RW) (b), and secondary-treatment wastewater effluent (WW) (c) under continuous dead-end mode using CN/F. Evolution of total organic carbon (TOC) removal was also included. d) Conversion of equivalent total carbon (X_{Ceq}), and e) pharmaceuticals in DW after adding specific anions (t = 3.5 h). $[Pharm.]_0$ = 3 μM each; $[Irrad.]_{avg}$ = 375 W·m^{-2}; τ = 100 min. Anions concentration (d and e, *according to WW values,* Table 1): $[SO_4^{2-}]$ = 0.39 mM; $[Cl^-]$ = 2.45 mM; and $[HCO_3^-]$ = 3.76 mM.

to some influence of their inherent constituents. For this reason, the effect of specific anions (such as SO_4^{2-}, Cl^-, and HCO_3^-, selected from those more representative from the WW sample) was evaluated in the photocatalytic conversion of both equivalent total carbon (Fig. 8**d**) and each specific pharmaceutical from the mixture (Fig. 8**e**). Overall, spiking SO_4^{2-} and Cl^- decreased the photocatalytic conversion (SO_4^{2-} at a higher extent due to the lower concentration used). This might be attributed to the generation of lower affinity radicals (*i.e.,* $SO_4^{\bullet-}$ and $HOCl^{\bullet-}$ by reacting with $HO^{\bullet}$ [76,77]). On the other hand, the presence of HCO_3^- allows a slight performance enhancement, probably related to the higher affinity of carbonate radical anion ($CO_3^{\bullet-}$) for amine fractions [78]. Indeed, and despite the simultaneous presence of other species may influence to a certain extent, this fact agrees with the previously proposed *Group I* (VFX, CTP, and TMD), characterized by the presence of terminal tertiary

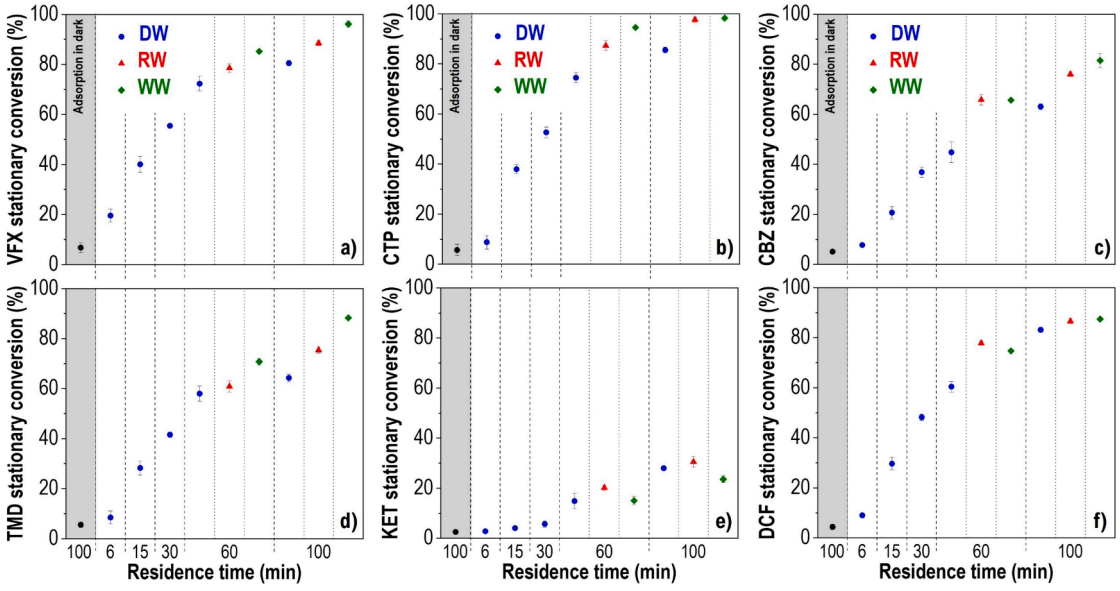

Fig. 9. Steady-state photocatalytic conversion of the pharmaceuticals VFX (a) CTP (b), CBZ (c), TMD (d), KET (e), and DCF (f) in mixture spiked in deionized water (DW), river water (RW), and secondary-treatment effluent from an urban wastewater treatment plant (WW) under continuous dead-end mode varying the hydraulic retention time (τ) using CN/F. $[Pharm.]_0$ = 3 μM each; $[Irrad.]_{avg}$ = 375 W·m^{-2}.

amines and depicting an improved elimination in the presence of HCO_3^-. As mentioned above, $HO^\bullet$ plays an important role in the oxidation mechanism of these compounds (see previous Fig. 7**b**), thus, it could be rationalized as a negative effect by the radical consumption in the presence of sulfate and chloride anions. Regarding *Group II*, the addition of HCO_3^- results in a slight conversion decrease for CBZ and DCF (presenting amine fractions different from terminal tertiary amines), and a remarkable inhibition effect on KET (characterized by the absence of any amine moiety). The contribution of these inorganic species, together with the likely influence of dissolved organic matter (*e.g.*, through photosensitization or generation of reactive intermediates under irradiation [75]), could eventually explain the improved performance in natural waters.

Effect of hydraulic retention time

Fig. 9 shows the steady-state conversion for each pharmaceutical achieved in the continuous treatment of the mixture spiked in the different aqueous matrices using τ values in the 6 to 100 min range. The removals determined in the absence of light (adsorption in the dark) under the highest τ value (100 min) were also included, in all cases being below 6% (with negligible differences among the investigated water matrices). The results suggest that to keep stationary overall conversions above 75% of pharmaceuticals contained in natural surface waters under continuous treatment mode (a feasible threshold value considering the potential use of this approach), the planar photoreactor on which the CN/F is supported should operate under hydraulic retention times ranging from 60 to 100 min. Lower τ values cannot allow enough contact between the irradiated photocatalyst and the contaminant, thus decreasing the removal yields rapidly, as commonly reported elsewhere [12,79].

In addition, **Table S5** summarizes the photocatalytic steady-state removals following the current reaction setup under τ of 100 and 60 min, being analogous to some of those previously reported immobilized photocatalysts in the continuous treatment of the same pharmaceuticals. As expected, our results are slightly lower when compared to combined processes of photocatalysis with ultrafiltration using TiO_2/PVDF film [80] or H_2O_2 addition using g-C_3N_4 immobilized onto ceramic foam [16]. In general terms, the film-immobilized CN evaluated in the current study demonstrated a remarkable performance for abating a series of pharmaceuticals in different water matrices, maintaining a stable activity under continuous recirculation and end-mode configurations. Furthermore, it is important to note that no significant changes (mainly related to modification of shape, dimensions, or general deterioration) were observed in the polymeric film (used to support the photocatalyst) after consecutive runs. Additionally, no increase in TOC was detected, suggesting that the polymeric support exhibited an acceptable level of stability under the conditions of this study.

3.3. Photocatalytic performance evaluation using EEM-PARAFAC methodology

When using natural water samples, it is also interesting to evaluate the effect of the photocatalytic treatment on other organic compounds inherently present in these aqueous matrices, namely naturally organic matter (NOM). For instance, some studies have evaluated the effectivity of different AOPs on NOM by EEM-PARAFAC analysis [81,82]. Therefore, EEM fluorescence spectroscopy was carried out in our study to learn about the evolution of dissolved organic matter with fluorescent properties. Previous studies [83–85] already reported the existence of five main regions (related to tyrosine-like (B), tryptophan-like (T), soluble microbial byproduct-like (M), fulvic-like (A), and humic-like substances (C)), distributed in three major groups (protein-like, microbial-like and humic-like compounds) [86] as summarized in Table 2, respecting the original regional nomenclature proposed by Coble [83]. Besides, Fig. S8**a-c** shows these fluorescent regions located over the EEM spectrum registered for the WW sample in our study. Although the main five regions can be observed in this sample, the highest intensities correspond to the regions of tryptophan-like substances (especially for those characterized at their highest λ_{ex} values, T1) and humic-like substances (C).

Fig. 10**a** shows the evolution of EEM fluorescence spectra under the continuous dead-end treatment using the film-immobilized CN. Before the beginning of the irradiation (0 h), it can be observed two main high-intensity bands at lower emission wavelengths (≈300 nm) compared to the tyrosine-like substances, ascribed to the addition of the mixture of pharmaceuticals, in agreement with the EEM spectra registered for each compound and collected in **Table S4**. In this respect, only VFX, CTP, and TMD (and DCF at weaker intensity) can be identified through fluorescence spectroscopy. Overall, the time progress in the irradiated stream shows the practical inhibition of the parent pharmaceuticals-related bands after 2 h, with an increasing signal of the regions concerning the T2 and A compounds (tryptophan- and fulvic-like substances, respectively), reaching a maximum after 4 h and subsequently decreases continuously, achieving a steady-state evolution after 8 h under continuous treatment. These bands can be ascribed to the pharmaceuticals-related byproducts, arising a formation-oxidation equilibrium after 6 h, which agrees with the evolution of TOC previously indicated.

Despite the maximum intensities of each region can be considered as an approach to evaluate the photocatalytic performance, a more rigorous procedure implies the deconvolution of EEM spectra and the determination of the intensity scores, including integrating several data points from each spectrum. Considering the set of all EEM spectra, up to five components were proposed, namely from Q1 to Q5 (characterized by their maximum $\lambda_{ex/em}$ values as shown in **Table S6** and **Figure S9**). The approximate location of the proposed compounds is depicted in Fig. 10**b**, agreeing with some of the main regions aforementioned (Table 2). The evolution of the regions ascribed to the original pharmaceuticals (and also the bands associated with tyrosine-like peaks) was not considered due to the likely interferences among both regions. Once the five proposed components were predicted, the evolution of their score was registered (Fig. 10**c**). Regarding the proteins-like substances, components Q1 and Q2 were related to the tryptophan-like substances of higher (T1) and lower (T2) λ_{ex} values, respectively. The initial score of Q1 decreased around 46% after achieving the steady-state conversion ($t \geq 6$h), suggesting a remarkable reduction in the content of these protein-based substances naturally present in the WW sample. On the other hand, Q2 depicted a continued increase of scores at the beginning of the photocatalytic treatment, peaking at 4 h and subsequently decreasing,

Table 2
Main regions, fluorescence excitation-emission wavelengths, and related compounds described in the literature (adapted from [83,86–88]). The compounds proposed in this study after PARAFAC analysis are also included.

Group	Region	Range $\lambda_{ex/em\ max}$ (nm)	Related compounds	Proposed compound in this study ($\lambda_{ex/em\ max}$ (nm))
Proteins	B1	(275–310/305–320)	Tyrosine-like	*Related to parent pharmaceuticals*
	B2	(220–237/305–320)		
	T1	(275–285/320–350)	Tryptophan-like	Q1 (282/341)
	T2	(215–237/340–381)		Q2 (242/368)
Microbial substances	M	(290–310/370–420)	Soluble microbial byproduct-like	Q3 (304/377)
Humic substances	A	(230–260/400–480)	Fulvic acid-like	Q4 (252/438)
	C	(320–360/420–460)	Humic acid-like	Q5 (356/434)

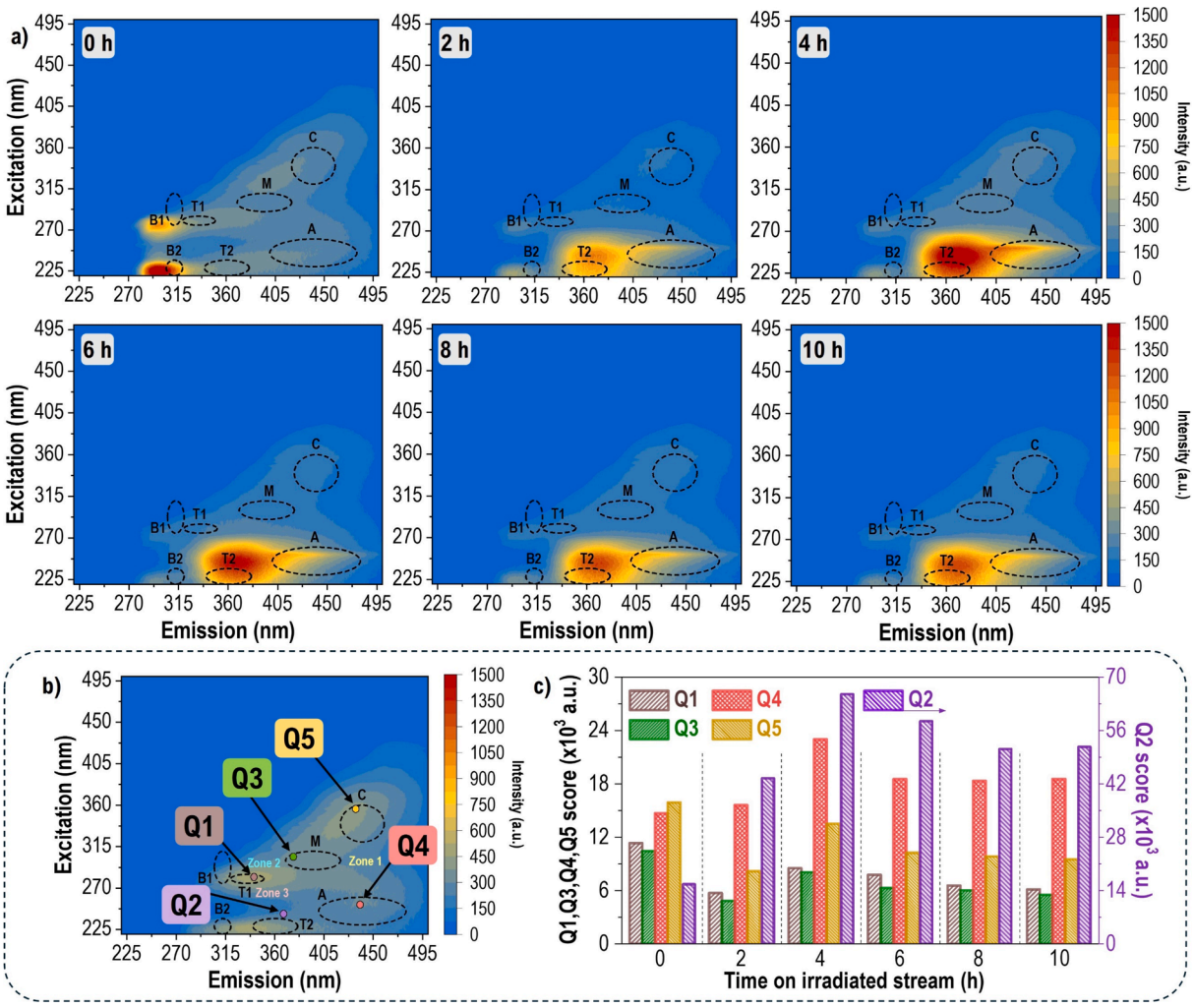

Fig. 10. A) Evolution of EEM fluorescent spectra, including the pharmaceuticals mixture spiked in WW under continuous dead-end mode using CN/F. The location (b) and score profiles under photocatalytic treatment (c) of the five proposed components (Q1-Q5) after PARAFAC modeling were included. $[Pharm.]_0 = 1.5$ μM each; $[Irrad.]_{avg} = 375$ W·m^{-2}, $\tau = 100$ min.

with a constant conversion close to 21% at the end of the continuous treatment. This evolution allows us to consider Q2 as one (or more than one) likely fluorescent byproduct from the conversion of the parent pharmaceuticals or the generation of molecular fluorophores from the transformation of tryptophan-like substances with analogous EEM fingerprints [81,89].

Concerning the other identified components, Q3, Q4, and Q5 were related to the soluble microbial byproduct-like, fulvic-like, and humic-like compounds, respectively. A similar trend (Fig. 10**c**) of the preceding Q2 was registered for Q4, which can be rationalized through the formation of fluorescent byproducts from the original pharmaceuticals (*e.g.,* see similarities related to the detection EEM spectrum of CBZ, **Table S4**), or even the generation of fulvic acids from the photocatalytic conversion of more complex structures related to the above-mentioned group of humic substances. A steady-state conversion of around 19% compared to the maximum value quantified after 4 h suggests that the current CN/F-mediated photocatalytic treatment allows the conversion of the compound (or compounds) herein identified as Q4. Moreover, Q3 and Q5 displayed a stationary decrease of around 47 and 40% of the initial score, respectively, proving a notable performance in eliminating NOM associated with microbial byproducts and humic acids. In this respect, Nguyen *et al.* [90] also reported the photocatalytic elimination of fluorescent organic matter contained in an aqueous sample from wastewater using ZnO under simulated solar light, highlighting the preferential removal of humic-like components compared to protein-like counterparts. Compared to that work, it should be noted that an immobilized photocatalyst and visible light sources were used in our study, thus representing an advantage considering the potential application of this approach. Therefore, and besides the pharmaceutical conversion proved in previous sections, the analysis of the EEM fluorescence spectra demonstrated that the photocatalytic treatment using CN/F allowed the removal of natural organic matter present in the matrix of a secondary-treatment effluent from an urban wastewater treatment plant, resulting a straightforward tool to assess the effectivity of the photocatalytic treatment.

4. Conclusions

Concerning the potential use of heterogeneous photocatalysis for the abatement of contaminants of emerging concern, this study proved the notable photocatalytic performance of carbon nitride immobilized on a polymeric film (CN/F) under visible light, aimed at applications of continuous treatment mode of wastewater streams using planar reactor configurations.

The activity of the CN/F was evaluated in both continuous flow total recirculation and dead-end regimes, showing remarkable stability of the supported material after long-term reuse. The total recirculation mode demonstrated the versatility of the photocatalyst for treating larger

water volumes without a noticeable decrease in the performance considering the equivalent irradiation time. Besides, up to five pharmaceuticals (including the antidepressants venlafaxine, citalopram, and carbamazepine, as well as the analgesics tramadol and diclofenac) were completely removed after 90 min, showing good conversion for other compounds with higher refractory character (as ketoprofen) despite the competition for the species with the highest contribution in the oxidation process (*i.e.,* photogenerated holes and superoxide radicals). The continuous dead-end mode evidenced the high continuous photocatalytic conversion of pharmaceuticals in a mixture using deionized water, whereas the removal rate in natural water samples (river and wastewater treatment plant effluent from Northern Portugal) incremented probably because of the presence of carbonate anions and organic matter. Indeed, the presence of chloride and sulfate anions yielded an inhibitory effect.

Concerning the potential application of this technological approach, adequate stationary conversion (above 75%) of pharmaceuticals in natural water samples was accomplished using hydraulic retention times between 60–100 min, with removal of total organic carbon of around 30%. Besides the conversion of pharmaceuticals, the effective conversion of naturally occurring fluorescent substances in the secondary-treatment wastewater effluent (humic-like, tryptophan-like, and soluble microbial byproducts-like compounds showing intensities reduction around 40–50%) was successfully proved using excitation/emission fluorescence spectroscopy, representing an excellent tool for validating the suitable performance of any photocatalyst for real environmental applications.

CRediT authorship contribution statement

Manuel Peñas-Garzón: Writing – review & editing, Writing – original draft, Methodology, Investigation, Formal analysis, Conceptualization. **Maria J. Sampaio:** Writing – review & editing, Validation, Methodology, Funding acquisition, Conceptualization. **Ana M. Chávez:** Writing – review & editing, Visualization, Methodology, Conceptualization. **Adrián M.T. Silva:** Writing – review & editing, Validation, Resources, Funding acquisition. **Cláudia G. Silva:** Writing – review & editing, Validation, Resources, Funding acquisition. **Joaquim L. Faria:** Writing – review & editing, Validation, Resources, Funding acquisition.

Declaration of competing interest

The authors declare that they have no known competing financial interests or personal relationships that could have appeared to influence the work reported in this paper.

Acknowledgments

This work was supported by national funds through FCT/MCTES (PIDDAC): LSRE-LCM, UIDB/50020/2020 (DOI: 10.54499/UIDB/50020/2020) and UIDP/50020/2020 (DOI: 10.54499/UIDP/50020/2020); and ALiCE, LA/P/0045/2020 (DOI: 10.54499/LA/P/0045/2020). Manuel Peñas-Garzón acknowledges his postdoctoral fellowship from Fundación Ramón Areces (XXXIV Convocatoria Ciencias de la Vida y de la Materia). Maria J. Sampaio acknowledges FCT funding under the Scientific Employment Stimulus - Institutional Call (DOI:10.54499/CEECINST/00010/2021/CP1770/CT0011). Ana M. Chávez is grateful to Ministerio de Universidades of Spain through Universidad de Extremadura (UEx) for her postdoctoral contract "Ayudas para la Recualificación del Sistema Universitario Español. Modalidad Margarita Salas" for young Ph.D. researchers (MS-17, UEX, call 2021) supported by European Union funds - NextGenerationEU. We are indebted to MSc Liliana Pereira from FEUP for her support in the characterization of water samples and TOC measurements. The SEM characterization services from CEMUP are also acknowledged.

Appendix A. Supplementary data

Supplementary data to this article can be found online at https://doi.org/10.1016/j.cej.2024.157384.

Data availability

Data will be made available on request.

References

[1] A. Hernández-Zanoletty, O. Cabezuelo, A. París-Reche, I. Oller, M.I. Polo-López, A. Agüera, P. Plaza, M.L. Marín, F. Boscá, S. Malato, Assessment of new immobilized photocatalysts based on TiO_2 for wastewater decontamination, J. Environ. Chem. Eng. 11 (6) (2023) 111291, https://doi.org/10.1016/j.jece.2023.111291.

[2] I. Grčić, N. Koprivanac, G. Li Puma, Modeling the photocatalytic oxidation of carboxylic acids on aqueous TiO_2 suspensions and on immobilized TiO_2-chitosan thin films in different reactor geometries irradiated by UVA or UVC light sources, Chemical Engineering Journal 422 (2021) 130104, https://doi.org/10.1016/j.cej.2021.130104.

[3] I.M. Sosnin, S. Vlassov, L.M. Dorogin, Application of polydimethylsiloxane in photocatalyst composite materials: A review, React. Funct. Polym. 158 (2021) 104781, https://doi.org/10.1016/j.reactfunctpolym.2020.104781.

[4] L.-T. Yen, C.-H. Weng, J.-H. Tzeng, Y.-C. Chen, A.R. Jacobson, Y.-T. Lin, Substantial improvement in photocatalysis performance of N-TiO_2 immobilized on PMMA: Exemplified by inactivation of Staphylococcus aureus and Escherichia coli, Sep. Purif. Technol. 345 (2024) 127298, https://doi.org/10.1016/j.seppur.2024.127298.

[5] L. Matoh, B. Žener, M. Kovačić, H. Kušić, I. Arčon, M. Levstek, U. Lavrenčič Štangar, Photocatalytic sol-gel/P25 TiO_2 coatings for water treatment: Degradation of 7 selected pharmaceuticals, Ceramics International 49(14, Part B) (2023) 24395-24406. https://doi.org/10.1016/j.ceramint.2022.09.204.

[6] W.-J. Ong, L.-L. Tan, Y.H. Ng, S.-T. Yong, S.-P. Chai, Graphitic Carbon Nitride (g-C_3N_4)-Based Photocatalysts for Artificial Photosynthesis and Environmental Remediation: Are We a Step Closer To Achieving Sustainability? Chem. Rev. 116 (12) (2016) 7159–7329, https://doi.org/10.1021/acs.chemrev.6b00075.

[7] Q. Zheng, A. Aiello, Y.S. Choi, K. Tarr, H. Shen, D.P. Durkin, D. Shuai, 3D printed photoreactor with immobilized graphitic carbon nitride: A sustainable platform for solar water purification, J. Hazard. Mater. 399 (2020) 123097, https://doi.org/10.1016/j.jhazmat.2020.123097.

[8] D. Hao, Q. Huang, W. Wei, X. Bai, B.-J. Ni, A reusable, separation-free and biodegradable calcium alginate/g-C_3N_4 microsphere for sustainable photocatalytic wastewater treatment, J. Clean. Prod. 314 (2021) 128033, https://doi.org/10.1016/j.jclepro.2021.128033.

[9] Z. Zhang, L. Zhang, Z. Huang, Y. Xu, Q. Zhao, H. Wang, M. Shi, X. Li, K. Jiang, D. Wu, "Floating Catalytic Foam" with prominent heat-induced convection for the effective photocatalytic removal of antibiotics, J. Hazard. Mater. 463 (2024) 132879, https://doi.org/10.1016/j.jhazmat.2023.132879.

[10] F. Wang, Z. Chen, Z. Zhu, J. Guo, Construction of visible light responsive ZnO/N-g-C_3N_4 composite membranes for antibiotics degradation, J. Mater. Res. Technol. 17 (2022) 1696–1706, https://doi.org/10.1016/j.jmrt.2022.01.140.

[11] J. Nieto-Sandoval, A. Torres-Pinto, M. Pedrosa, M. Munoz, Z.M. de Pedro, C. G. Silva, J.L. Faria, J.A. Casas, A.M.T. Silva, Application of g-C_3N_4-PVDF membrane for the photocatalytic degradation of micropollutants in continuous flow mode: Impact of water matrix, J. Environ. Chem. Eng. 11 (5) (2023) 110586, https://doi.org/10.1016/j.jece.2023.110586.

[12] N.F.F. Moreira, M.J. Sampaio, A.R. Ribeiro, C.G. Silva, J.L. Faria, A.M.T. Silva, Metal-free g-C_3N_4 photocatalysis of organic micropollutants in urban wastewater under visible light, Appl Catal B 248 (2019) 184–192, https://doi.org/10.1016/j.apcatb.2019.02.001.

[13] M. Pedrosa, M.J. Sampaio, T. Horvat, O.C. Nunes, G. Dražić, A.E. Rodrigues, J. L. Figueiredo, C.G. Silva, A.M.T. Silva, J.L. Faria, Visible-light-induced self-cleaning functional fabrics using graphene oxide/carbon nitride materials, Appl. Surf. Sci. 497 (2019) 143757, https://doi.org/10.1016/j.apsusc.2019.143757.

[14] R.A. Fernandes, M.J. Sampaio, G. Dražić, J.L. Faria, C.G. Silva, Efficient removal of parabens from real water matrices by a metal-free carbon nitride photocatalyst, Sci. Total Environ. 716 (2020) 135346, https://doi.org/10.1016/j.scitotenv.2019.135346.

[15] M. Peñas-Garzón, M.J. Sampaio, Y. Manrique, C.G. Silva, J.L. Faria, Enhanced removal of emerging pollutants through visible light-activated carbon nitride materials immobilized over 3D printed structures, J. Environ. Chem. Eng. 11 (6) (2023) 111343, https://doi.org/10.1016/j.jece.2023.111343.

[16] A.M. Chávez, A. Torres-Pinto, P.M. Álvarez, J.L. Faria, C.G. Silva, A.M.T. Silva, One-pot synthesis and immobilization of urea-derived graphitic carbon nitride onto ceramic foams for visible-light photocatalytic wet peroxide oxidation in water treatment, Chem. Eng. J. 481 (2024) 148141, https://doi.org/10.1016/j.cej.2023.148141.

[17] M.J. Sampaio, A.R.L. Ribeiro, C.M.R. Ribeiro, R.A. Borges, M.F. Pedrosa, A.M. T. Silva, C.G. Silva, J.L. Faria, A technological approach using a metal-free immobilized photocatalyst for the removal of pharmaceutical substances from urban wastewaters, Chem. Eng. J. 459 (2023) 141617, https://doi.org/10.1016/j.cej.2023.141617.

[18] L. Paredes, S. Murgolo, H. Dzinun, M.H. Dzarfan Othman, A.F. Ismail, M. Carballa, G. Mascolo, Application of immobilized TiO_2 on PVDF dual layer hollow fibre membrane to improve the photocatalytic removal of pharmaceuticals in different water matrices, Applied Catalysis b: Environmental 240 (2019) 9–18, https://doi.org/10.1016/j.apcatb.2018.08.067.

[19] O. Vieira, R.S. Ribeiro, M. Pedrosa, A.R. Lado Ribeiro, A.M.T. Silva, Nitrogen-doped reduced graphene oxide – PVDF nanocomposite membrane for persulfate activation and degradation of water organic micropollutants, Chemical Engineering Journal 402 (2020) 126117, https://doi.org/10.1016/j.cej.2020.126117.

[20] H.B. Truong, B.T. Huy, Y.-I. Lee, H.T. Nguyen, J. Cho, J. Hur, Magnetic visible-light activated photocatalyst $CuFe_2O_4/Bi_2WO_6$/mpg-C_3N_4 for the treatment of natural organic matter, Chem. Eng. J. 453 (2023) 139777, https://doi.org/10.1016/j.cej.2022.139777.

[21] T.T. Nguyen, S.N. Nam, Sunlight-driven photocatalysis of dissolved organic matter: Tracking by excitation emission matrix-parallel factor analysis and optimization using response surface methodology, Environ. Eng. Res. 26 (3) (2021) https://doi.org/110.4491/eer.2020.201.

[22] Y. Han, Z. Zhu, C. Hu, J. Zheng, B. Liu, W. Wang, 3D flower-like Cu-BiOCl/Bi_2S_3 heterostructure with synergistic Cu ion doping: A study on efficient tetracycline degradation under visible light, Colloids Surf A Physicochem Eng Asp 683 (2024) 133014, https://doi.org/10.1016/j.colsurfa.2023.133014.

[23] F.J. Rodríguez-Vidal, M. García-Valverde, B. Ortega-Azabache, Á. González-Martínez, A. Bellido-Fernández, Using excitation-emission matrix fluorescence to evaluate the performance of water treatment plants for dissolved organic matter removal, Spectrochim. Acta A Mol. Biomol. Spectrosc. 249 (2021) 119298, https://doi.org/10.1016/j.saa.2020.119298.

[24] H.B. Truong, I. Rabani, B.T. Huy, N.H.T. Tran, J. Hur, Using floating photocatalyst mpg-C_3N_4/expanded perlite to treat natural organic matter under visible light, Chem. Eng. J. 466 (2023) 143178, https://doi.org/10.1016/j.cej.2023.143178.

[25] C. Castillo-Zacarías, M.E. Barocio, E. Hidalgo-Vázquez, J.E. Sosa-Hernández, L. Parra-Arroyo, I.Y. López-Pacheco, D. Barceló, H.N.M. Iqbal, R. Parra-Saldívar, Antidepressant drugs as emerging contaminants: Occurrence in urban and non-urban waters and analytical methods for their detection, Sci. Total Environ. 757 (2021) 143722, https://doi.org/10.1016/j.scitotenv.2020.143722.

[26] M.-K. Nguyen, C. Lin, X.-T. Bui, M.R.J. Rakib, H.-L. Nguyen, Q.-M. Truong, H.-G. Hoang, H.-T. Tran, G. Malafaia, A.M. Idris, Occurrence and fate of pharmaceutical pollutants in wastewater: Insights on ecotoxicity, health risk, and state–of–the-art removal, Chemosphere 354 (2024) 141678, https://doi.org/10.1016/j.chemosphere.2024.141678.

[27] M.J. Lima, A.M.T. Silva, C.G. Silva, J.L. Faria, Graphitic carbon nitride modified by thermal, chemical and mechanical processes as metal-free photocatalyst for the selective synthesis of benzaldehyde from benzyl alcohol, J. Catal. 353 (2017) 44–53, https://doi.org/10.1016/j.jcat.2017.06.030.

[28] J. Tauc, Absorption edge and internal electric fields in amorphous semiconductors, Mater. Res. Bull. 5 (8) (1970) 721–729, https://doi.org/10.1016/0025-5408(70)90112-1.

[29] J. Liu, Origin of High Photocatalytic Efficiency in Monolayer g-C_3N_4/CdS Heterostructure: A Hybrid DFT Study, J. Phys. Chem. C 119 (51) (2015) 28417–28423, https://doi.org/10.1021/acs.jpcc.5b09092.

[30] P.E. Laranjeira, A.A. Martins, M.I. Nunes, J.C.B. Lopes, M.M. Dias, NETmix®, a new type of static mixer: Experimental characterization and model validation, AIChE J 57 (4) (2011) 1020–1032, https://doi.org/10.1002/aic.12316.

[31] V.M.T.M. Silva, P.A. Quadros, P.E.M.S.C. Laranjeira, M.M. Dias, J.C.B. Lopes, A Novel Continuous Industrial Process for Producing Hydroxyapatite Nanoparticles, Journal of Dispersion Science and Technology 29(4) (2008) 542-547. https://doi.org/10.1080/01932690701728924.

[32] M.J. Lima, A.M.T. Silva, C.G. Silva, J.L. Faria, J.C.B. Lopes, M.M. Dias, An innovative static mixer photoreactor: Proof of concept, Chem. Eng. J. 287 (2016) 419–424, https://doi.org/10.1016/j.cej.2015.09.092.

[33] B.A. Marinho, R. Djellabi, R.O. Cristóvão, J.M. Loureiro, R.A.R. Boaventura, M. M. Dias, J.C.B. Lopes, V.J.P. Vilar, Intensification of heterogeneous TiO_2 photocatalysis using an innovative micro–meso-structured-reactor for Cr(VI) reduction under simulated solar light, Chem. Eng. J. 318 (2017) 76–88, https://doi.org/10.1016/j.cej.2016.05.077.

[34] M.J. Lima, M.E. Leblebici, M.M. Dias, J.C.B. Lopes, C.G. Silva, A.M.T. Silva, J. L. Faria, Continuous flow photo-Fenton treatment of ciprofloxacin in aqueous solutions using homogeneous and magnetically recoverable catalysts, Environ. Sci. Pollut. Res. 21 (19) (2014) 11116–11125, https://doi.org/10.1007/s11356-014-2515-6.

[35] A. Singh, D. Saidulu, A.K. Gupta, V. Kubsad, Occurrence and fate of antidepressants in the aquatic environment: Insights into toxicological effects on the aquatic life, analytical methods, and removal techniques, J. Environ. Chem. Eng. 10 (6) (2022) 109012, https://doi.org/10.1016/j.jece.2022.109012.

[36] A. Shaliutina-Kolešová, O. Shaliutina, R. Nian, The effects of environmental antidepressants on macroinvertebrates: a mini review, Water and Environment Journal 34 (1) (2020) 153–159, https://doi.org/10.1111/wej.12448.

[37] Off. J. Eur. Union (2022). Commission implementing decision (EU) 2022/1307 of 22 July 2022.

[38] M.J. Sampaio, C.G. Silva, A.M.T. Silva, J.L. Faria, Kinetic modelling for the photocatalytic degradation of phenol by using TiO_2-coated glass raschig rings under simulated solar light, J. Chem. Technol. Biotechnol. 91 (2) (2016) 346–352, https://doi.org/10.1002/jctb.4571.

[39] M. Jiménez-Salcedo, M. Monge, M.T. Tena, Study of intermediate by-products and mechanism of the photocatalytic degradation of ciprofloxacin in water using graphitized carbon nitride nanosheets, Chemosphere 247 (2020) 125910, https://doi.org/10.1016/j.chemosphere.2020.125910.

[40] R.P. Cavalcante, R.F. Dantas, B. Bayarri, O. González, J. Giménez, S. Esplugas, A. Machulek, Photocatalytic mechanism of metoprolol oxidation by photocatalysts TiO_2 and TiO_2 doped with 5% B: Primary active species and intermediates, Appl Catal B 194 (2016) 111–122, https://doi.org/10.1016/j.apcatb.2016.04.054.

[41] A. Torres-Pinto, A.M. Díez, C.G. Silva, J.L. Faria, M.Á. Sanromán, A.M.T. Silva, M. Pazos, Photoelectrocatalytic degradation of pharmaceuticals promoted by a metal-free g-C_3N_4 catalyst, Chem. Eng. J. 476 (2023) 146761, https://doi.org/10.1016/j.cej.2023.146761.

[42] G.V. Buxton, C.L. Greenstock, W.P. Helman, A.B. Ross, Critical Review of rate constants for reactions of hydrated electrons, hydrogen atoms and hydroxyl radicals (·OH/·O− in Aqueous Solution, J. Phys. Chem. Ref. Data 17 (2) (1988) 513–886, https://doi.org/10.1063/1.555805.

[43] A. Samuni, C.M. Krishna, J.B. Mitchell, C.R. Collins, A. Russo, Superoxide Reaction with Nitroxides, Free Radic. Res. Commun. 9 (3–6) (1990) 241–249, https://doi.org/10.3109/10715769009145682.

[44] A.P.H. Association, A.W.W. Association, W. Federation, Standard methods for the examination of water and wastewater, American Public Health Association Washington, DC, USA, 2005.

[45] F.A. Chiappini, M.R. Alcaraz, H.C. Goicoechea, A.C. Olivieri, A graphical user interface as a new tool for scattering correction in fluorescence data, Chemom. Intel. Lab. Syst. 193 (2019) 103810, https://doi.org/10.1016/j.chemolab.2019.07.009.

[46] S. Elcoroaristizabal, R. Bro, J.A. García, L. Alonso, PARAFAC models of fluorescence data with scattering: A comparative study, Chemom. Intel. Lab. Syst. 142 (2015) 124–130, https://doi.org/10.1016/j.chemolab.2015.01.017.

[47] F.A. Chiappini, A. Muñoz de la Peña, H.C. Goicoechea, A.C. Olivieri, An upgrade of MVC2, a MATLAB graphical user interface for second-order multivariate calibration: Beyond trilinear models, Chemom. Intel. Lab. Syst. 237 (2023) 104814, https://doi.org/10.1016/j.chemolab.2023.104814.

[48] M.H. Kamstrup-Nielsen, L.G. Johnsen, R. Bro, Core consistency diagnostic in PARAFAC2, J. Chemom. 27 (5) (2013) 99–105, https://doi.org/10.1002/cem.2497.

[49] A. Torres-Pinto, C.G. Silva, J.L. Faria, A.M.T. Silva, The effect of precursor selection on the microwave-assisted synthesis of graphitic carbon nitride, Catal. Today 424 (2023) 113868, https://doi.org/10.1016/j.cattod.2022.08.010.

[50] R. Li, X. Cui, J. Bi, X. Ji, X. Li, N. Wang, Y. Huang, X. Huang, H. Hao, Urea-induced supramolecular self-assembly strategy to synthesize wrinkled porous carbon nitride nanosheets for highly-efficient visible-light photocatalytic degradation, RSC Adv. 11 (38) (2021) 23459–23470, https://doi.org/10.1039/D1RA03524J.

[51] D.R. Paul, R. Sharma, S.P. Nehra, A. Sharma, Effect of calcination temperature, pH and catalyst loading on photodegradation efficiency of urea derived graphitic carbon nitride towards methylene blue dye solution, RSC Adv. 9 (27) (2019) 15381–15391, https://doi.org/10.1039/C9RA02201E.

[52] P. Gibot, F. Schnell, D. Spitzer, Enhancement of the graphitic carbon nitride surface properties from calcium salts as templates, Microporous Mesoporous Mater. 219 (2016) 42–47, https://doi.org/10.1016/j.micromeso.2015.07.026.

[53] Z. Zeng, D. Yu, Z. He, J. Liu, F.-X. Xiao, Y. Zhang, R. Wang, D. Bhattacharyya, T.T. Y. Tan, Graphene Oxide Quantum Dots Covalently Functionalized PVDF Membrane with Significantly-Enhanced Bactericidal and Antibiofouling Performances, Sci. Rep. 6 (1) (2016) 20142, https://doi.org/10.1038/srep20142.

[54] I.S. Elashmawi, N.A. Hakeem, Effect of PMMA addition on characterization and morphology of PVDF, Polym. Eng. Sci. 48 (5) (2008) 895–901, https://doi.org/10.1002/pen.21032.

[55] R. Binjhade, R. Mondal, S. Mondal, Continuous photocatalytic reactor: Critical review on the design and performance, J. Environ. Chem. Eng. 10 (3) (2022) 107746, https://doi.org/10.1016/j.jece.2022.107746.

[56] S. Mozia, Photocatalytic membrane reactors (PMRs) in water and wastewater treatment, A Review, Separation and Purification Technology 73 (2) (2010) 71–91, https://doi.org/10.1016/j.seppur.2010.03.021.

[57] T.T. Guaraldo, R. Vakili, J. Wenk, D. Mattia, Highly efficient ZnO photocatalytic foam reactors for micropollutant degradation, Chem. Eng. J. 455 (2023) 140784, https://doi.org/10.1016/j.cej.2022.140784.

[58] N. Chekir, D. Tassalit, O. Benhabiles, N. Sahraoui, M. Mellal, Effective removal of paracetamol in compound parabolic collectors and fixed bed reactors under natural sunlight, Water Sci. Technol. 82 (11) (2020) 2460–2471, https://doi.org/10.2166/wst.2020.511.

[59] I. Grčić, G. Li Puma, Six-flux absorption-scattering models for photocatalysis under wide-spectrum irradiation sources in annular and flat reactors using catalysts with different optical properties, Applied Catalysis b: Environmental 211 (2017) 222–234, https://doi.org/10.1016/j.apcatb.2017.04.014.

[60] N. Mokhtari, A.R. Solaimany Nazar, M. Farhadian, P. Eskandari, B. Jeon, Silver deposition on titanium oxide thin glass films for efficient visible light-induced photocatalytic removal of diphenhydramine and venlafaxine, International Journal of Environmental Science and Technology 19(12) (2022) 12465-12476. https://doi.org/10.1007/s13762-022-04486-0.

[61] I. Velo-Gala, A. Torres-Pinto, C.G. Silva, B. Ohtani, A.M.T. Silva, J.L. Faria, Graphitic carbon nitride photocatalysis: the hydroperoxyl radical role revealed by kinetic modelling, Cat. Sci. Technol. 11 (23) (2021) 7712–7726, https://doi.org/10.1039/D1CY01657A.

[62] S. Samanta, S. Khilari, D. Pradhan, R. Srivastava, An Efficient, Visible Light Driven, Selective Oxidation of Aromatic Alcohols and Amines with O_2 Using $BiVO_4$/g-C_3N_4 Nanocomposite: A Systematic and Comprehensive Study toward the Development of a Photocatalytic Process, ACS Sustain. Chem. Eng. 5 (3) (2017) 2562–2577, https://doi.org/10.1021/acssuschemeng.6b02902.

[63] X. Li, J. Yu, M. Jaroniec, Hierarchical photocatalysts, Chem. Soc. Rev. 45 (9) (2016) 2603–2636, https://doi.org/10.1039/C5CS00838G.
[64] D. Wegstein, A. Zaim, B.O. Burek, J.Z. Bloh, The Importance of Precise Reaction Condition Control for the Comparison of Photocatalyst Materials on the Example of Hydrogen Peroxide Formation over Polymeric Carbon Nitrides, ChemPhotoChem 7 (11) (2023) e202300095.
[65] J. Alom, M.S. Hasan, M. Asaduzaman, M.T. Alam, D. Belhaj, R. Selvaraj, M. A. Hossain, M. Zargar, M.B. Ahmed, Catalytical Performance of Heteroatom Doped and Undoped Carbon-Based Materials, Catalysts 13 (5) (2023) 823, https://doi.org/10.3390/catal13050823.
[66] L. Wang, Q. Zhang, B. Chen, Y. Bu, Y. Chen, J. Ma, F.L. Rosario-Ortiz, R. Zhu, Some issues limiting photo(cata)lysis application in water pollutant control: A critical review from chemistry perspectives, Water Res 174 (2020) 115605, https://doi.org/10.1016/j.watres.2020.115605.
[67] P.M. Wood, The potential diagram for oxygen at pH 7, Biochem. J 253 (1) (1988) 287–289, https://doi.org/10.1042/bj2530287.
[68] N. Rioja, S. Zorita, F.J. Peñas, Effect of water matrix on photocatalytic degradation and general kinetic modeling, Appl Catal B 180 (2016) 330–335, https://doi.org/10.1016/j.apcatb.2015.06.038.
[69] M. Peñas-Garzón, M.J. Sampaio, Y.L. Wang, J. Bedia, J.J. Rodriguez, C. Belver, C. G. Silva, J.L. Faria, Solar photocatalytic degradation of parabens using UiO-66-NH_2, Sep. Purif. Technol. 286 (2022) 120467, https://doi.org/10.1016/j.seppur.2022.120467.
[70] M. Cai, S. Gowrisankaran, M. Gregor, H. Makarov, T. Roch, J. Li, F. Wu, G. Mailhot, M. Brigante, O. Monfort, Unravelling the activation mechanism of oxidants using copper ferrite nanopowder and its application in the treatment of real waters contaminated by phenolic compounds, Chem. Eng. J. 481 (2024) 148623, https://doi.org/10.1016/j.cej.2024.148623.
[71] A.M. Chávez, D.H. Quiñones, A. Rey, F.J. Beltrán, P.M. Álvarez, Simulated solar photocatalytic ozonation of contaminants of emerging concern and effluent organic matter in secondary effluents by a reusable magnetic catalyst, Chem. Eng. J. 398 (2020) 125642, https://doi.org/10.1016/j.cej.2020.125642.
[72] Y. Zhang, J. Zhang, Y. Xiao, V.W.C. Chang, T.-T. Lim, Direct and indirect photodegradation pathways of cytostatic drugs under UV germicidal irradiation: Process kinetics and influences of water matrix species and oxidant dosing, J. Hazard. Mater. 324 (2017) 481–488, https://doi.org/10.1016/j.jhazmat.2016.11.016.
[73] A.R. Lado Ribeiro, N.F.F. Moreira, G. Li Puma, A.M.T. Silva, Impact of water matrix on the removal of micropollutants by advanced oxidation technologies, Chemical Engineering Journal 363 (2019) 155–173, https://doi.org/10.1016/j.cej.2019.01.080.
[74] Z. Lin, Z. Wang, Z. Xu, Z. Xiao, Z. Fang, J. Luo, P. Li, P. Chen, W. Lv, G. Liu, Self-assembly construction of 1D carbon nitride nanotubes and cobalt-modified for superior photocatalytic degradation of sulfonamide antibiotics, Chemosphere 343 (2023) 140299, https://doi.org/10.1016/j.chemosphere.2023.140299.
[75] Y. Guo, Z. Guo, J. Wang, Z. Ye, L. Zhang, J. Niu, Photodegradation of three antidepressants in natural waters: Important roles of dissolved organic matter and nitrate, Sci. Total Environ. 802 (2022) 149825, https://doi.org/10.1016/j.scitotenv.2021.149825.
[76] T. Li, X. Wang, Y. Chen, J. Liang, L. Zhou, Producing $^{\cdot}OH$, $SO_4^{\cdot-}$ and $O_2^{\cdot-}$ in heterogeneous Fenton reaction induced by Fe_3O_4-modified schwertmannite, Chem. Eng. J. 393 (2020) 124735, https://doi.org/10.1016/j.cej.2020.124735.
[77] M.L. Djaballah, A. Belghit, A. Dehane, S. Merouani, O. Hamdaoui, M. Ashokkumar, Radicals ($^{\cdot}OH$, $Cl^{\cdot}$, $ClO^{\cdot}$ and $Cl_2^{\cdot-}$) concentration profiles in the intensified degradation of reactive green 12 by UV/chlorine process: Chemical kinetic analysis using a validated model, J. Photochem. Photobiol. A Chem. 439 (2023) 114557, https://doi.org/10.1016/j.jphotochem.2023.114557.
[78] Y. Huang, M. Kong, D. Westerman, E.G. Xu, S. Coffin, K.H. Cochran, Y. Liu, S. D. Richardson, D. Schlenk, D.D. Dionysiou, Effects of HCO_3^- on Degradation of Toxic Contaminants of Emerging Concern by UV/NO_3, Environ Sci Technol 52 (21) (2018) 12697–12707, https://doi.org/10.1021/acs.est.8b04383.
[79] S. Sarkar, S. Chakraborty, C. Bhattacharjee, Photocatalytic degradation of pharmaceutical wastes by alginate supported TiO_2 nanoparticles in packed bed photo reactor (PBPR), Ecotoxicologyand Environmental Safety 121 (2015) 263–270, https://doi.org/10.1016/j.ecoenv.2015.02.035.
[80] K. Szymański, J. Grzechulska-Damszel, S. Mozia, Application of a submerged photocatalytic membrane reactor with ultrafiltration membrane for ketoprofen removal during long term process: Impact of feed matrix, J. Water Process Eng. 59 (2024) 104953, https://doi.org/10.1016/j.jwpe.2024.104953.
[81] I. Sciscenko, A. Arques, P. Micó, M. Mora, S. García-Ballesteros, Emerging applications of EEM-PARAFAC for water treatment: a concise review, Chemical Engineering Journal Advances 10 (2022) 100286, https://doi.org/10.1016/j.ceja.2022.100286.
[82] Z. Chen, M. Li, Q. Wen, N. Ren, Evolution of molecular weight and fluorescence of effluent organic matter (EfOM) during oxidation processes revealed by advanced spectrographic and chromatographic tools, Water Res. 124 (2017) 566–575, https://doi.org/10.1016/j.watres.2017.08.006.
[83] P.G. Coble, Characterization of marine and terrestrial DOM in seawater using excitation-emission matrix spectroscopy, Mar. Chem. 51 (4) (1996) 325–346, https://doi.org/10.1016/0304-4203(95)00062-3.
[84] W. Chen, P. Westerhoff, J.A. Leenheer, K. Booksh, Fluorescence Excitation−Emission Matrix Regional Integration to Quantify Spectra for Dissolved Organic Matter, Environ. Sci. Technol. 37 (24) (2003) 5701–5710, https://doi.org/10.1021/es034354c.
[85] K. Song, Y. Shang, Z. Wen, P.-A. Jacinthe, G. Liu, L. Lyu, C. Fang, Characterization of CDOM in saline and freshwater lakes across China using spectroscopic analysis, Water Res. 150 (2019) 403–417, https://doi.org/10.1016/j.watres.2018.12.004.
[86] F.J. Rodríguez-Vidal, Application of Excitation-Emission Matrix Fluorescence (EEMF) in the Wastewater Field, in: P. Raffaello (Ed.), Fluorescence Imaging, IntechOpen, Rijeka, 2022, p. Ch. 2. https://doi.org/10.5772/intechopen.105975.
[87] W.-T. Li, S.-Y. Chen, Z.-X. Xu, Y. Li, C.-D. Shuang, A.-M. Li, Characterization of Dissolved Organic Matter in Municipal Wastewater Using Fluorescence PARAFAC Analysis and Chromatography Multi-Excitation/Emission Scan: A Comparative Study, Environ. Sci. Technol. 48 (5) (2014) 2603–2609, https://doi.org/10.1021/es404624q.
[88] A. Huguet, L. Vacher, S. Relexans, S. Saubusse, J.M. Froidefond, E. Parlanti, Properties of fluorescent dissolved organic matter in the Gironde Estuary, Org Geochem. 40 (6) (2009) 706–719, https://doi.org/10.1016/j.orggeochem.2009.03.002.
[89] J. Schneider, C.J. Reckmeier, Y. Xiong, M. von Seckendorff, A.S. Susha, P. Kasák, A. L. Rogach, Molecular Fluorescence in Citric Acid-Based Carbon Dots, J. Phys. Chem. C 121 (3) (2017) 2014–2022, https://doi.org/10.1021/acs.jpcc.6b12519.
[90] T.T. Nguyen, S.N. Nam, J. Oh, Photo-Transformation of Effluent Organic Matter by ZnO-Based Sunlight Irradiation, Appl. Sci. 10 (24) (2020) 9002, https://doi.org/10.3390/app10249002.